1

TADF Material Design: Photophysical Background and Case Studies Focusing on Cu(I) and Ag(I) Complexes[a]

Hartmut Yersin[1,b], *Rafał Czerwieniec*[1], *Marsel Z. Shafikov*[1,2], *and Alfiya F. Suleymanova*[1]

[1] *University of Regensburg, Department of Chemistry, Institute of Physical Chemistry, Universitätsstr. 31, Regensburg, D-93053, Germany*
[2] *Ural Federal University, Department of Technology of Organic Synthesis, Institute of Chemical Technology, Mira str. 19, Ekaterinburg, 620002, Russia*

1.1 Introduction

Basic research of photophysical and chemical properties of organo-transition metal compounds was strongly activated by their potential commercial use. This became particularly apparent for classes of compounds that may be applied as emitters in organic light-emitting diodes (OLEDs) [1–19] or in light emitting electrochemical cells (LEEC) [7, 20–28]. These scientific investigations led to a much deeper understanding of the photophysical principles and of the compound's properties resulting in the development of an enormous number of new materials in part with drastically improved properties for OLED applications [4, 9, 29–52]. Improvements were also stimulated in the fields of related functional materials based on metal complexes for sensing of oxygen or temperature [53–59] or for photocatalysis [60–66].

For luminescent materials to be applied in OLEDs, it is essential that all excitons generated in the emission layer are harvested and converted into photons. Since the statistic ratio of the formed excitons is 1 singlet to 3 triplets [67, 68], special mechanisms that allow to harvest all of them are required, as the two types of excitons show different relaxation properties [67]. Already about 20 years ago, it was discovered that third-row transition metal complexes, especially those with Ir(III), Pt(II), or Os(II) metal centers, are well suited for such harvesting processes, since the metal centers can induce efficient spin–orbit coupling (SOC) [69–77] between the lowest triplet state T_1 and higher-lying singlet states S_n (with $n > 1$) [1, 9, 11, 12, 67, 69–89]. As a consequence, fast intersystem crossing (ISC) to the lowest triplet state of several tens of femtosecond [88, 90] can occur, and relatively high radiative phosphorescent rates from the T_1 state to the electronic

[a] Previously published in ChemPhysChem, 2017, 18, 3508–3535 with permission by Wiley-VCH.
[b] Author for correspondence: ORCID ID: http://orcid.org/0000-0003-3216-1370.

Highly Efficient OLEDs: Materials Based on Thermally Activated Delayed Fluorescence,
First Edition. Edited by Hartmut Yersin.

ground state S_0 are induced. These latter rates can become as high as $\approx 10^6$ s^{-1} [70, 89, 91]. Therefore, these phosphorescent compounds are frequently denoted as triplet emitters. As a consequence, when applied in OLEDs, these materials can harvest all singlet and triplet excitons in the lowest excited triplet state. Accordingly, the corresponding mechanism is denoted as *triplet harvesting effect* [69, 78]. Indeed, using, for example, $Ir(ppy)_3$ (with ppy = 2-phenylpyridinate), OLEDs with almost 100% internal quantum efficiency could be produced [11, 81].

However, these triplet emitter complexes require high-cost rare metals, and this may become a limiting factor, when OLED lighting goes into mass production [70, 92, 93]. Therefore, an alternative harvesting mechanism that may work with low-cost materials has been proposed more than one decade ago [94]. This mechanism is based on the molecular effect of thermally activated delayed fluorescence (TADF), according to which also all excitons generated in the emission layer may be harvested. In this situation, however, the emission does not stem from the lowest excited triplet state, but from the thermally activated singlet state S_1. Hence, this mechanism has been denoted as *singlet harvesting mechanism* [9, 30, 31, 37, 40, 56, 70, 92, 94–97]. Accordingly, the luminescent materials do not need to contain high SOC-inducing metal centers (high-cost materials), since the (thermally activated) singlet state usually carries sufficient allowedness with respect to the transition to the singlet ground state (spin-allowed transition). Therefore, an efficient path for photon generation becomes available.

Obviously, thermal activation, from the lowest triplet state T_1 to the higher-lying singlet state S_1, requires a relatively small energy separation $\Delta E(S_1–T_1)$ between these states. For example, at ambient temperature ($T = 300$ K), a thermal energy of $k_B T \approx 210\ cm^{-1}$ (26 meV) is available (k_B = Boltzmann constant). Hence, as a rule of thumb, efficient thermal activation with fast up-ISC or reverse intersystem crossing (rISC) is not expected to occur for $\Delta E(S_1–T_1)$ distinctly above 10^3 cm^{-1} ($\approx$130 meV). Indeed, such energy separations can be realized with environmentally friendly and low-cost Cu(I) [4, 9, 27, 30–35, 37–56, 70, 92, 93, 95–105] and Ag(I) [104, 106–109] complexes as well as with purely organic molecules [110–113].

In this review, we focus on Cu(I) and Ag(I) complexes. For these materials, we have to address three crucial photophysical requirements:

1) The emitter compounds should exhibit high photoluminescence quantum yields ϕ_{PL}. After an electronic excitation, however, Cu(I) and Ag(I) complexes experience distinct flattening distortions with respect to the ground state geometries [114–123]. Usually, such geometry changes are related to an increase of nonradiative deactivation or even result in total quenching of the luminescence by vibrational relaxation. This is induced by a strong increase of the Franck–Condon factors of the low-lying vibrational modes of the excited electronic state and highly excited vibrational modes of the electronic ground state [124–126]. However, these shortcomings may be suppressed to a large extent by rigidifying the molecular structure either by sterically demanding ligands or by a rigid environment. This behavior has already been discussed frequently in the literature [9, 30, 31, 35, 92, 95, 96, 108, 109, 114, 119, 127]. We will address these properties in Sections 1.3 and 1.6. Interestingly, design of a material, a silver complex, with Φ_{PL} of 100% becomes possible

by following this strategy of rigidifying the molecular structure (see Refs [108, 109] and Section 1.6).

2) Well-designed TADF materials should exhibit relatively small energy separations $\Delta E(S_1–T_1)$. For organo-transition metal compounds, this is related to the occurrence of metal-to-ligand charge-transfer (MLCT) (and ligand-to-ligand charge-transfer (LL'CT)) states having frontier orbitals, highest occupied molecular orbital (HOMO) and lowest unoccupied molecular orbital (LUMO), which are spatially largely separated. This leads to a small exchange interaction [128–130] between the involved electrons and, hence, to the required small splitting between the singlet S_1 and triplet T_1 state. In particular, a relatively small $\Delta E(S_1–T_1)$ value is a necessary condition to obtain a short radiative TADF decay time, which is important to maximize the photoluminescence quantum yield Φ_{PL}. Moreover, for use in OLEDs, short decay times are important to minimize roll-off effects (for example, induced by saturation or triplet-polaron quenching) and to reduce device stability problems as well as undesired energy transfer processes from the emitter dopant to the host. In Sections 1.3 and 1.4, discussing case studies, we will present Cu(I) compounds and the dependence of photophysical properties on the $\Delta E(S_1–T_1)$ gap.
3) The TADF properties crucially depend on the allowedness of the $S_1 \rightarrow S_0$ fluorescence that is thermally activated from the lower-lying triplet state. The reason is that the corresponding radiative rate $k_r(S_1 \rightarrow S_0)$ also governs the TADF decay time. $k_r(S_1 \rightarrow S_0)$ should be as large as possible to obtain a short TADF decay time. However, basic quantum chemical considerations show that these rates $k_r(S_1 \rightarrow S_0)$ and $\Delta E(S_1–T_1)$ correlate. We address this behavior in Section 1.5.

Thus, designing of TADF compounds with short TADF decay time and high emission quantum yield is a challenge. For example, radiative TADF decay times of Cu(I) complexes of less than 3–5 μs have not been reported so far [30, 31, 96]. We will discuss this challenge in several sections of this investigation. In particular, in Section 1.6, where we focus on designing new Ag(I) complexes, we will show how to develop a breakthrough TADF material [108, 109] with a radiative TADF decay time of only 1.4 μs (at $\phi_{PL} = 100\%$), which is significantly shorter than so far reported.

This chapter is organized as follows: In Section 1.2, we introduce different parameters that have to be addressed for designing efficient TADF materials based on Cu(I) and Ag(I) complexes, and we present the materials studied in this chapter together with selected photophysical data. Sections 1.3 and 1.4 display case studies of Cu(I) complexes with large and small $\Delta E(S_1–T_1)$ energy separation, respectively. Furthermore, we discuss effects of SOC with respect to properties of the lowest triplet state, such as phosphorescence allowedness and zero-field splitting (ZFS). In Section 1.5, we show on a very simple quantum mechanical basis that the size of the energy gap $\Delta E(S_1–T_1)$ and the allowedness of the singlet $S_1 \rightarrow$ singlet S_0 transition are correlated. This result is clearly supported by experimental data. In Section 1.6, we present photophysical properties of a new TADF class of Ag(I) complexes, and we show how an extraordinarily efficient TADF material can be designed. Finally, in a conclusion, we will give a short summary and point to future perspectives.

1.2 TADF, Molecular Parameters, and Diversity of Materials

The molecular TADF effect was already reported more than five decades ago [131, 132]. It can be described by the use of Figure 1.1. By an optical excitation, one usually excites a singlet state, for example, higher-lying vibrational levels of the S_1 state. Subsequently, fast vibrational relaxation of the order of 10^{-12} s [124] proceeds to lower lying vibrational levels. Then, depending on the class of molecules, prompt fluorescence and/or down-ISC (as well as nonradiative relaxation to the electronic ground state) can occur. For Cu(I) and Ag(I) complexes, being in the focus of this contribution, ISC from S_1 to the T_1 state is very effective, since fast ISC occurring in the time range of 3–30 ps has been observed [118, 121, 122, 133, 134]. The individual value does not only depend on molecular properties, for example, on the extent of SOC of higher-lying singlets to the lowest triplet state, but also on the local environment, such as a fluid or a rigid matrix [134]. In general, a significant prompt fluorescence ($S_1 \rightarrow S_0$) is not detected, instead a very bright long-lived phosphorescence ($T_1 \rightarrow S_0$) is frequently observed at low temperature [30, 31, 33–35, 70, 92, 95–97, 135, 136]. At a higher temperature and in a situation of a fast thermal equilibration, population of the higher-lying singlet state is governed by the Boltzmann distribution. In this context, "fast" means that the down- and up-ISC processes are much faster than the $T_1 \rightarrow S_0$ and $S_1 \rightarrow S_0$ emission decay processes. As a consequence, the emission decays with a single decay time being a weighted average (Eq. (1.1)) of the $T_1 \rightarrow S_0$ and $S_1 \rightarrow S_0$ decay processes. Usually, this is fulfilled for Cu(I) and Ag(I) complexes with low-lying MLCT states. At lower temperatures population of the S_1 state due to the Boltzmann thermal distribution is frozen out. For completeness, it is remarked that below $T \approx 15$ K, effects of spin–lattice relaxation (SLR) between the triplet substates might strongly slow down relaxation processes [31, 33, 34, 88, 95, 137–139]. Consequently, frequently a multiexponential decay (from the different T_1 substates to the ground state S_0) is observed at very low temperature.

At higher temperatures, up-ISC processes efficiently depopulate the triplet T_1 state, i.e. the three triplet substates, and populate the singlet S_1 state. In particular, if the emission decay time of the T_1 state is long, for example, longer than several 100 μs, the phosphorescence is largely "quenched" and almost only the $S_1 \rightarrow S_0$ fluorescence is observed. Because the population of the S_1 state is fed from the long-living triplet state (triplet reservoir), this type of fluorescence is also long living compared with the prompt fluorescence that does not involve a triplet state. Hence, the emission is denoted as TADF.

For completeness, it is mentioned that for several Cu(I) complexes, SOC with respect to the T_1 state is significant. In this situation, the TADF process will not fully deplete the T_1 state during its much shorter population time, and a combined TADF/phosphorescence is observed. This property is not in the focus of the present contribution, but is discussed in detail in the literature [31, 33, 34, 97].

In the emission layer of an OLED device, the electron-hole recombination produces excitons of different spin multiplicity, that is, 75% are of triplet and 25% of

singlet character [67, 68, 78, 79] (Figure 1.1). These excitons can be trapped in the emitter molecule. Such mechanisms are discussed in Ref. [67]. Subsequently, fast internal conversions, i.e. one singlet path and three triplet paths, populate the S_1 and the T_1 state, respectively [67]. Then similarly to the behavior after optical excitation, thermal activation takes place. In particular, in a situation of a forbidden $T_1 \rightarrow S_0$ transition and a relatively small $\Delta E(S_1–T_1)$ value, finally almost all excitations are transferred to the lowest excited singlet state, which then exhibits delayed $S_1 \rightarrow S_0$ fluorescence. According to this process, the molecular TADF effect as exploited in an OLED device has been denoted as *singlet harvesting mechanism* [9, 30, 31, 70, 94–96].

As already stressed, the TADF decay time τ(TADF) should be as short as possible (obviously, at a high emission quantum yield), if the emitter is applied in an OLED. To achieve this goal, valuable guidelines can be deduced. Especially, a discussion of the temperature dependence of the emission decay time is helpful. This is easily explained by the use of a model discussion of a simplified molecule with two excited states, a singlet S_1 and a triplet T_1, being in fast thermal equilibrium, and the electronic ground state S_0 (compare Figure 1.1). In this situation, the

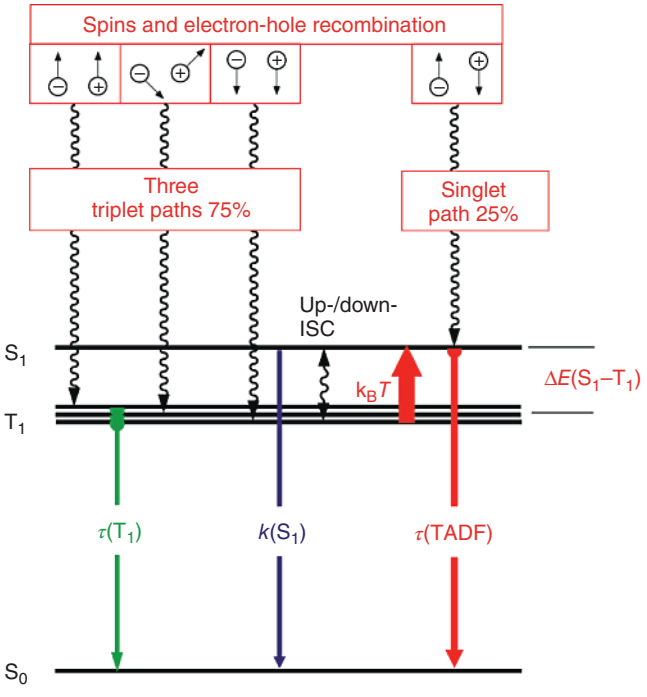

Figure 1.1 Illustration of the molecular TADF effect and its use in OLEDs (singlet harvesting). $\tau(T_1)$ and τ(TADF) are the phosphorescence decay time and the TADF decay time, respectively. $k(S_1) = k_r(S_1 \rightarrow S_0)$ is the radiative rate of the $S_1 \rightarrow S_0$ transition (prompt fluorescence). Up-ISC is also often denoted as reverse intersystem crossing (rISC).

decay time $\tau(T)$ of the luminescent molecule is described by a Boltzmann-type relation [30] (compare also [140–143]):

$$\tau(T) = \frac{3 + \exp\left(-\frac{\Delta E(S_1 - T_1)}{k_B T}\right)}{3k(T_1) + k(S_1)\exp\left(-\frac{\Delta E(S_1 - T_1)}{k_B T}\right)} \tag{1.1}$$

$k(T_1) = 1/\tau(T_1)$ and $k(S_1) = 1/\tau(S_1)$ are the decay rates with the decay times $\tau(T_1)$ and $\tau(S_1)$ of the triplet and singlet excited state, respectively, and $\Delta E(S_1 - T_1)$ is the energy separation between the S_1 and T_1 state. $\tau(T)$ represents the experimentally accessible emission decay time at a given temperature. For the subsequent discussion, it is assumed that the molecular parameters $\tau(T_1)$, $\tau(S_1)$, and $\Delta E(S_1 - T_1)$ are temperature independent and that the splitting of the triplet state into three substates (ZFS) is small, i.e. much smaller than $k_B T$.

Thus, application of Eq. (1.1) to the measured decay times at different temperatures opens access to the molecular parameters given above. In particular, it becomes possible to determine very small energy separations being much below the attainable spectral resolution. For example, using a slightly modified Eq. (1.1) energy separations of only a few cm^{-1} can be resolved despite the fact that the MLCT emission bands are frequently as broad as several thousand cm^{-1} (compare [9, 31, 95, 97, 140]).

At very low temperature, the exponential terms in Eq. (1.1) are negligible, and the measured decay time $\tau(T)$ displays the phosphorescence decay time $\tau(T_1)$, while at high temperature (and long $\tau(T_1)$), the term containing $\tau(T_1)$ can be neglected, and one obtains essentially the decay time τ(TADF). In Sections 1.3, 1.4, and 1.6, several case studies, discussing the $\tau(T)$ temperature behavior, are presented.

Eq. (1.1) shows that three parameters crucially determine the emission decay time. These parameters can be deduced from fitting Eq. (1.1) to the measured emission decay times for a suitable temperature range. If this is carried out for a number of Cu(I) and/or Ag(I) complexes, valuable guidelines for molecular design rules can be extracted. Therefore, a more detailed discussion of the three parameters is illustrative.

Figure 1.2 schematically visualizes the photophysical background of the parameters that govern Eq. (1.1). For all three cases, subsequently discussed in detail, it is assumed that the respective molecule shows TADF.

1.2.1 TADF and Phosphorescence

Figure 1.2a displays an energy level diagram of a compound that exhibits significant SOC of the triplet state T_1 to a singlet state. Quantum mechanical considerations show that SOC between the triplet state T_1 and the singlet state S_1 both stemming from the same orbital configuration vanishes [9, 30, 31, 69–77]. However, mixing in of different, higher-lying singlets S_n (with $n > 1$) can be significant. If so, the triplet state of Cu(I) complexes, for example, exhibits a distinct ZFS of several cm^{-1} (a few 0.1 meV), and the $T_1 \rightarrow S_0$ transition rate for the phosphorescence can become as large as $5 \times 10^4\ s^{-1}$ (20 µs) [30, 34, 97, 135, 136].

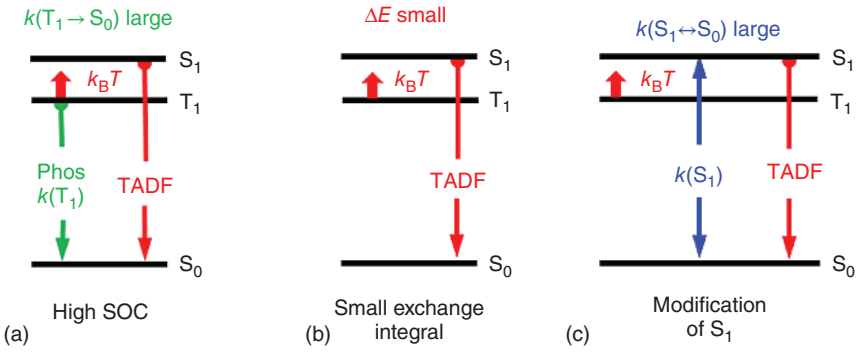

Figure 1.2 Different strategies for minimizing the emission decay time of TADF compounds for OLED applications. The zero-field splitting of the T_1 state into three substates is not shown in this diagram.

Accordingly, a second, effective radiative decay channel is opened in addition to the TADF decay path. These combined radiative decay paths can distinctly shorten the ambient temperature emission decay time. In this contribution, we do not focus further on this effect, but compare the literature reports [30, 31, 34, 97, 144].

1.2.2 Minimizing $\Delta E(S_1–T_1)$

As already addressed, the energy separation $\Delta E(S_1–T_1)$ between the lowest singlet S_1 and triplet state T_1 should be relatively small (Figure 1.2b). This can be well achieved with Cu(I) and Ag(I) complexes, if the lowest lying excited states are largely of ^{1,3}MLCT character. In this situation, a distinct charge separation between the unpaired electrons can occur. As a consequence, the quantum mechanical exchange interaction [128–130] and, hence, also the singlet–triplet splitting becomes small (Section 1.5). Because $\Delta E(S_1–T_1)$ enters in an exponential term in Eq. (1.1), $\Delta E(S_1–T_1)$ reduction has a dominating effect on the TADF decay time, τ(TADF). However, this seems to be limited, when $\Delta E(S_1–T_1)$ becomes lower than 200–300 cm^{-1} (25 to ≈40 meV), since at smaller splitting, decrease of the $S_1–S_0$ transition rate $k_r(S_1 \rightarrow S_0)$ might induce an opposite trend and lead to an increase of τ(TADF). (In Section 1.5 it will be shown that $\Delta E(S_1–T_1)$ and $k_r(S_1 \rightarrow S_0)$ are related to each other.) The variation of $\Delta E(S_1–T_1)$ can be achieved by a suitable molecular design as discussed below in this section and in the case studies presented in the next two sections.

1.2.3 Importance of $k_r(S_1–S_0)$

The allowedness of the $S_1 \leftrightarrow S_0$ transition can be expressed, for example, by the radiative fluorescence rate $k_r(S_1 \rightarrow S_0)$ (Figure 1.2c). According to Eq. (1.1), this rate also plays an important role at determining the TADF decay time. Frequently, this property is not adequately addressed. The rate should be as high as possible to obtain short TADF decay time. For this requirement also $\Delta E(S_1–T_1)$ should

be as small as possible. However, the two photophysical parameters are correlated. Small splitting $\Delta E(S_1–T_1)$ requires a small exchange interaction between the unpaired electrons, at least when both T_1 and S_1 states are well described by a HOMO–LUMO excitation. For a small exchange interaction, small overlap of HOMO and LUMO is advantageous. At the same time, small HOMO–LUMO overlap leads to a small oscillator strength (small allowedness) of the $S_1 \rightarrow S_0$ transition and, thus, to a small $k_r(S_1 \rightarrow S_0)$ value and, hence, to a long fluorescence decay time. Indeed, experimental studies on Cu(I) complexes exhibiting TADF reveal that such a correlation exists for a large number of compounds (compare also Section 1.5) [31].

However, it is indicated that a close correlation between these two photophysical properties might not always be so strict. In particular, the S_1 state might be modified by a suitable molecular design. For example, quantum mechanical configuration interaction (CI) can be helpful in this respect. This means that a different, higher-lying singlet state, which is energetically proximate and carries high allowedness (high oscillator strength) with respect to the transition to the electronic ground state, can mix with the S_1 state and induce a higher $S_1 \rightarrow S_0$ allowedness. Presumably, this mechanism is important for the Ag(I) complexes discussed in Section 1.6.

Experimental access to the photophysical parameters as discussed above and in Figure 1.2 becomes possible by the use of a fitting procedure of Eq. (1.1) to the measured values of $\tau(T)$ over a large temperature range. The required range depends on the size of $\Delta E(S_1–T_1)$. For example, if $\Delta E(S_1–T_1)$ values are larger than about $700\,cm^{-1}$ (87 meV), a temperature range of $77\,K \leq T \leq 300\,K$ might usually be sufficient. However, for smaller splittings, the range has to be extended, for example, to $T = 30\,K$ to be able to characterize a compound with a splitting of only $\Delta E(S_1–T_1) = 370\,cm^{-1}$ (compound **2**, see Section 1.4) [31, 96]. Moreover, if the splitting of the T_1 state into substates of a few cm^{-1} (a few 0.1 meV) and the corresponding photophysical properties should be addressed, extension of the temperature range to about $T = 1.3\,K$ (and application of a slightly modified Eq. (1.1)) is required [58, 70, 88, 89, 97, 138, 145].

In Sections 1.3, 1.4, and 1.6, we will present case studies. In these we will show how to develop a deeper understanding of representative compounds. In Table 1.1, for a broader overview, we summarize a selection of photophysical data for a large number of complexes that are addressed in this contribution. The compounds studied were investigated as powder materials. In this respect, it should be remarked that very frequently, the decay behavior measured of powder materials is modified, for example, by processes of energy transfer or triplet–triplet annihilation. However, if the low-lying charge-transfer (CT) states of the complexes exhibit geometry distortions also in the relatively rigid crystalline environment, localization (self-trapping) can occur and prevent energy transfer effects. Thus, the emission of the powder material can display molecular properties. Accordingly, concentration quenching does not occur, and the decay behavior does not show any distinctive feature (such as shortening of decay times) with concentration increase [30, 31, 58, 95].

Table 1.1 Photophysical data based on luminescence measurements of powder materials arranged according to increasing $\Delta E(S_1–T_1)$.

Compound	Photophysical data	References
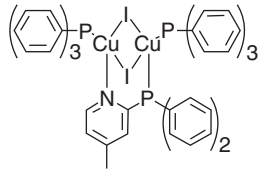 $Cu_2I_2(MePyrPHOS)(Pph_2)_2$ **1**	$\Delta E(S_1–T_1) = 270\ cm^{-1}$ $\lambda_{max}(300\ K) = 511\ nm$ $\Phi_{PL}(300\ K) = 97\%$ $\tau(300\ K) = 5\ \mu s$ $\tau(T_1 \rightarrow S_0) = 23\ \mu s$ $\tau(S_1 \rightarrow S_0) = 570\ ns$	[31, 38]
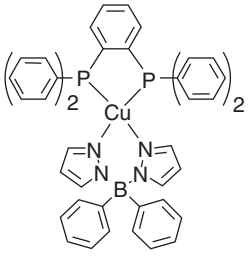 Cu(dppb)(pz_2Bph_2) **2**	$\Delta E(S_1–T_1) = 370\ cm^{-1}$ $\lambda_{max}(300\ K) = 535\ nm$ $\Phi_{PL}(300\ K) = 70\%$ $\tau(300\ K) = 3.3\ \mu s$ $\tau(T_1 \rightarrow S_0) = 1200\ \mu s$ $\tau(S_1 \rightarrow S_0) = 180\ ns$	[43, 96, 146]
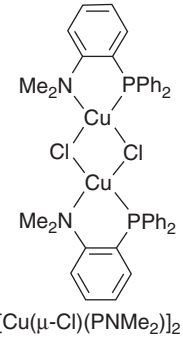 $[Cu(\mu\text{-}Cl)(PNMe_2)]_2$ **3**	$\Delta E(S_1–T_1) = 460\ cm^{-1}$ $\lambda_{max}(300\ K) = 506\ nm$ $\Phi_{PL}(300\ K) = 45\%$ $\tau(300\ K) = 6.6\ \mu s$ $\tau(T_1 \rightarrow S_0) = 250\ \mu s$ $\tau(S_1 \rightarrow S_0) = 210\ ns$	[33]
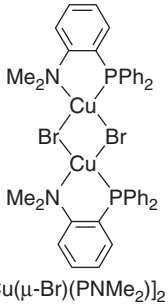 $[Cu(\mu\text{-}Br)(PNMe_2)]_2$ **4**	$\Delta E(S_1–T_1) = 510\ cm^{-1}$ $\lambda_{max}(300\ K) = 490\ nm$ $\Phi_{PL}(300\ K) = 65\%$ $\tau(300\ K) = 4.1\ \mu s$ $\tau(T_1 \rightarrow S_0) = 1200\ \mu s$ $\tau(S_1 \rightarrow S_0) = 110\ ns$	[33]

(Continued)

Table 1.1 (Continued)

Compound	Photophysical data	References
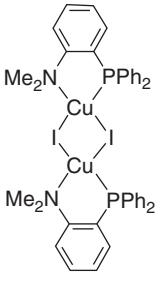 [Cu(μ-I)(PNMe$_2$)]$_2$ **5**	$\Delta E(S_1–T_1) = 570\ cm^{-1}$ $\lambda_{max}(300\ K) = 464\ nm$ $\Phi_{PL}(300\ K) = 65\%$ $\tau(300\ K) = 4.6\ \mu s$ $\tau(T_1 \rightarrow S_0) = 290\ \mu s$ $\tau(S_1 \rightarrow S_0) = 90\ ns$	[33]
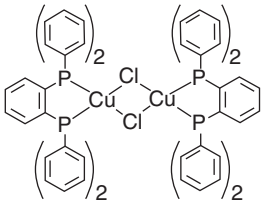 $Cu_2Cl_2(dppb)_2$ **6**	$\Delta E(S_1–T_1) = 600\ cm^{-1}$ $\lambda_{max}(300\ K) = 545\ nm$ $\Phi_{PL}(300\ K) = 35\%$ $\tau(300\ K) = 3\ \mu s$ $\tau(T_1 \rightarrow S_0) = 2200\ \mu s$ $\tau(S_1 \rightarrow S_0) = 70\ ns$	[100, 107]
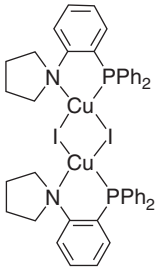 [Cu(μ-I)(PNpy)]$_2$ **7**	$\Delta E(S_1–T_1) = 630\ cm^{-1}$ $\lambda_{max}(300\ K) = 465\ nm$ $\Phi_{PL}(300\ K) = 65\%$ $\tau(300\ K) = 5.6\ \mu s$ $\tau(T_1 \rightarrow S_0) = 250\ \mu s$ $\tau(S_1 \rightarrow S_0) = 100\ ns$	[33]
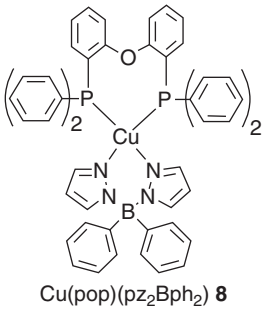 Cu(pop)(pz$_2$Bph$_2$) **8**	$\Delta E(S_1–T_1) = 650\ cm^{-1}$ $\lambda_{max}(300\ K) = 464\ nm$ $\Phi_{PL}(300\ K) = 90\%$ $\tau(300\ K) = 13\ \mu s$ $\tau(T_1 \rightarrow S_0) = 500\ \mu s$ $\tau(S_1 \rightarrow S_0) = 170\ ns$	[9, 95, 147, 148]

Table 1.1 (Continued)

Compound	Photophysical data	References
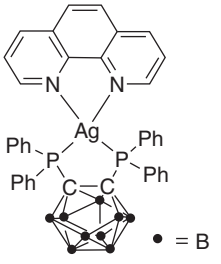 Ag(phen)(P_2-nCB) **9**	$\Delta E(S_1-T_1)$ –[a] λ_{max}(300 K) = 575 nm Φ_{PL}(300 K) = 36% τ(300 K) = 2 μs τ(77 K) = 270 μs $\tau(S_1 \rightarrow S_0)$ –	[109] Table 1.7
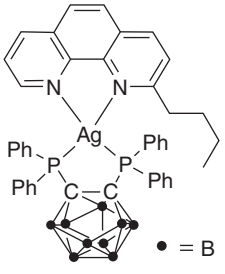 Ag(mbp)(P_2-nCB) **10**	$\Delta E(S_1-T_1)$ = 640 cm^{-1} λ_{max}(300 K) = 535 nm Φ_{PL}(300 K) = 70% τ(300 K) = 2 μs $\tau(T_1 \rightarrow S_0)$ = 1600 μs $\tau(S_1 \rightarrow S_0)$ = 32 ns	[109] Table 1.7
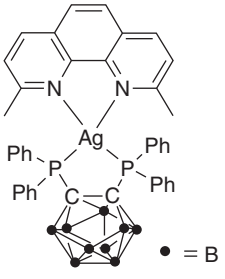 Ag(dmp)(P_2-nCB) **11**	$\Delta E(S_1-T_1)$ = 650 cm^{-1} λ_{max}(300 K) = 537 nm Φ_{PL}(300 K) = 78% τ(300 K) = 2.8 μs $\tau(T_1 \rightarrow S_0)$ = 890 μs $\tau(S_1 \rightarrow S_0)$ = 36 ns	[109] Table 1.6
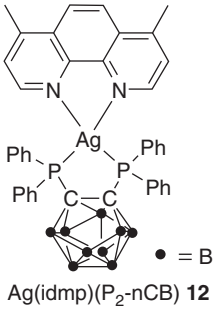 Ag(idmp)(P_2-nCB) **12**	$\Delta E(S_1-T_1)$[a] λ_{max}(300 K) = 562 nm Φ_{PL}(300 K) = 45% τ(300 K) = 1.7 μs $\tau(T_1 \rightarrow S_0)$ = 475 μs	[109]

(Continued)

Table 1.1 (Continued)

Compound	Photophysical data	References
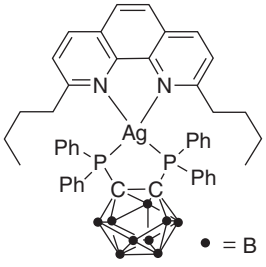 Ag(dbp)(P_2-nCB) **13**	$\Delta E(S_1-T_1) = 650\ cm^{-1}$ $\lambda_{max}(300\ K) = 526\ nm$ $\Phi_{PL}(300\ K) = 100\%$ $\tau(300\ K) = 1.4\ \mu s$ $\tau(T_1 \rightarrow S_0) = 1570\ \mu s$ $\tau(S_1 \rightarrow S_0) = 18\ ns$	[108, 109]
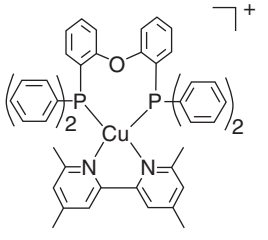 Cu(tmbpy)(pop)$^+$ **14**[b]	$\Delta E(S_1-T_1) = 720\ cm^{-1}$ $\lambda_{max}(300\ K) = 555\ nm$ $\Phi_{PL}(300\ K) = 55\%$ $\tau(300\ K) = 11\ \mu s$ $\tau(T_1 \rightarrow S_0) = 84\ \mu s$ $\tau(S_1 \rightarrow S_0) = 160\ ns$	[35]
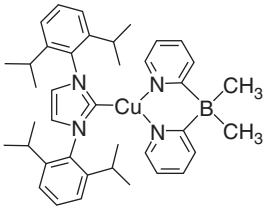 (IPr)Cu(py_2-BMe_2) **15**	$\Delta E(S_1-T_1) = 740\ cm^{-1}$ $\lambda_{max}(300\ K) = 475\ nm$ $\Phi_{PL}(300\ K) = 76\%$ $\tau(300\ K) = 11\ \mu s$ $\tau(T_1 \rightarrow S_0) = 34\ \mu s$ $\tau(S_1 \rightarrow S_0) = 160\ ns$	[34, 149]
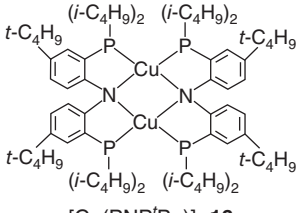 [Cu(PNP^{t}Bu)]$_2$ **16**	$\Delta E(S_1-T_1) = 786\ cm^{-1}$ $\lambda_{max}(300\ K) = 512\ nm$ $\Phi_{PL}(300\ K) = 57\%$ $\tau(300\ K) = 11\ \mu s$ $\tau(T_1 \rightarrow S_0) = 343\ \mu s$ $\tau(S_1 \rightarrow S_0) = 79\ ns$	[46]

Table 1.1 (Continued)

Compound	Photophysical data	References
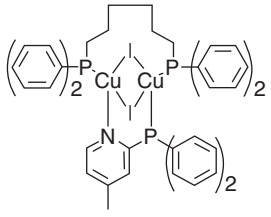 Cu_2I_2(MePyrPHOS)(dpph) **17**	$\Delta E(S_1–T_1) = 830\ cm^{-1}$ $\lambda_{max}(300\ K) = 519\ nm$ $\Phi_{PL}(300\ K) = 88\%$ $\tau(300\ K) = 24\ \mu s$ $\tau(T_1 \rightarrow S_0) = 110\ \mu s$ $\tau(S_1 \rightarrow S_0) = 190\ ns$	[30, 41]
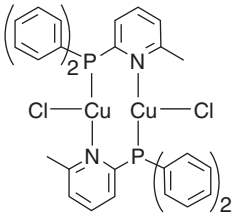 Cu_2Cl_2(N^P)$_2$ **18**	$\Delta E(S_1–T_1) = 930\ cm^{-1}$ $\lambda_{max}(300\ K) = 485\ nm$ $\Phi_{PL}(300\ K) = 92\%$ $\tau(300\ K) = 8.3\ \mu s$ $\tau(T_1 \rightarrow S_0) = 42\ \mu s$ $\tau(S_1 \rightarrow S_0) = 40\ ns$	[96, 150]
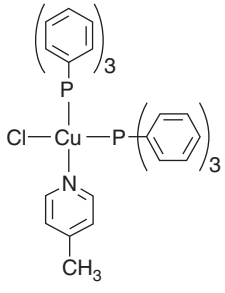 $CuCl(Pph_3)_2$(4-Mepy) **19**	$\Delta E(S_1–T_1) = 940\ cm^{-1}$ $\lambda_{max}(300\ K) = 468\ nm$ $\Phi_{PL}(300\ K) = 99\%$ $\tau(300\ K) = 9.4\ \mu s$ $\tau(T_1 \rightarrow S_0) = 34\ \mu s$ $\tau(S_1 \rightarrow S_0) = 47\ ns$	[98]
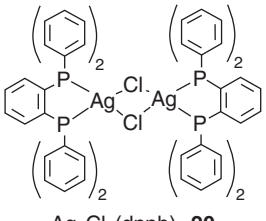 $Ag_2Cl_2(dppb)_2$ **20**	$\Delta E(S_1–T_1) = 980\ cm^{-1}$ $\lambda_{max}(300\ K) = 480\ nm$ $\Phi_{PL}(300\ K) = 93\%$ $\tau(300\ K) = 15\ \mu s$ $\tau(T_1 \rightarrow S_0) = 1100\ \mu s$ $\tau(S_1 \rightarrow S_0) = 45\ ns$	[107]

(Continued)

Table 1.1 (Continued)

Compound	Photophysical data	References
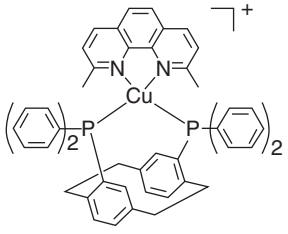 Cu(dmp)(phanephos)$^+$ **21**[c]	$\Delta E(S_1–T_1) = 1000\ cm^{-1}$ $\lambda_{max}(300\ K) = 530\ nm$ $\Phi_{PL}(300\ K) = 80\%$ $\tau(300\ K) = 14\ \mu s$ $\tau(T_1 \rightarrow S_0) = 240\ \mu s$ $\tau(S_1 \rightarrow S_0) = 40\ ns$	[92, 151]
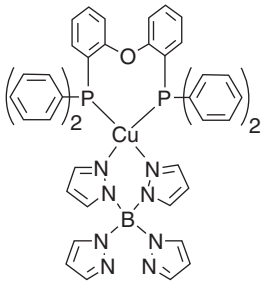 Cu(pop)(pz_4B) **22**	$\Delta E(S_1–T_1) = 1000\ cm^{-1}$ $\lambda_{max}(300\ K) = 447\ nm$ $\Phi_{PL}(300\ K) = 90\%$ $\tau(300\ K) = 22\ \mu s$ $\tau(T_1 \rightarrow S_0) = 450\ \mu s$ $\tau(S_1 \rightarrow S_0) = 80\ ns$	[95, 148]
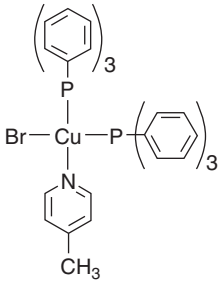 $CuBr(Pph_3)_2$(4-Mepy) **23**	$\Delta E(S_1–T_1) = 1070\ cm^{-1}$ $\lambda_{max}(300\ K) = 467\ nm$ $\Phi_{PL}(300\ K) = 95\%$ $\tau(300\ K) = 15\ \mu s$ $\tau(T_1 \rightarrow S_0) = 50\ \mu s$ $\tau(S_1 \rightarrow S_0) = 41\ ns$	[98]
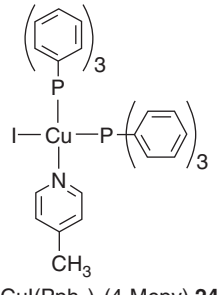 $CuI(Pph_3)_2$(4-Mepy) **24**	$\Delta E(S_1–T_1) = 1170\ cm^{-1}$ $\lambda_{max}(300\ K) = 455\ nm$ $\Phi_{PL}(300\ K) = 66\%$ $\tau(300\ K) = 9.5\ \mu s$ $\tau(T_1 \rightarrow S_0) = 49\ \mu s$ $\tau(S_1 \rightarrow S_0) = 14\ ns$	[98]

Table 1.1 (Continued)

Compound	Photophysical data	References
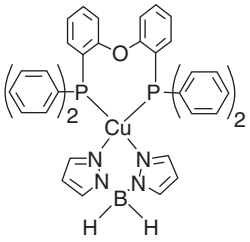 Cu(pop)(pz_2BH_2) **25**	$\Delta E(S_1-T_1) = 1300\ cm^{-1}$ $\lambda_{max}(300\ K) = 436\ nm$ $\Phi_{PL}(300\ K) = 45\%$ $\tau(300\ K) = 20\ \mu s$ $\tau(T_1 \rightarrow S_0) = 610\ \mu s$ $\tau(S_1 \rightarrow S_0) = 10\ ns$	[70, 95, 148]

$\Delta E(S_1-T_1)$ and $\tau(S_1 \rightarrow S_0)$ values result from fitting procedures. A prompt fluorescence of the S_1 state has not been observed directly.

a) Similar $\Delta E(S_1-T_1)$ values are expected to occur for all Ag(phen-substituted)(P_2-nCB) complexes displayed in this table.
b) Investigated as [Cu(tmbpy)(pop)](BF_4) powder.
c) Investigated as [Cu(dmp)(phanephos)](PF_6) powder.

Source: Ref. [31]. Reproduced with permission of Elsevier.

1.3 Case Study: TADF of a Cu(I) Complex with Large $\Delta E(S_1-T_1)$

The luminescence properties of TADF compounds depend strongly on the energy separation between the lowest excited singlet and triplet state. In this case study, we discuss properties of Cu(dmp)(phanephos)$^+$ **21** (with dmp = 2,9-dimethyl-1,10-phenanthroline and phanephos = 4,12-bis(diphenylphosphino)-[2.2]-paracyclophane) (Figure 1.3).

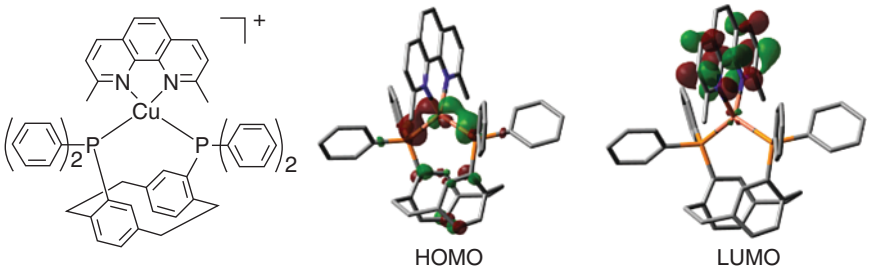

Figure 1.3 Chemical formula and frontier orbitals of Cu(dmp)(phanephos)$^+$ **21** obtained for the DFT-optimized triplet state (T_1) geometry. The calculations were performed at the B3LYP/def2-SVP level of theory [152, 153]. Hydrogen atoms are omitted for clarity. HOMO and LUMO exhibit distinctly different spatial distributions. The HOMO is mainly composed of the copper 3d and phosphorus sp^3 atomic orbitals, while the LUMO represents essentially a π^* orbital of the dmp ligand.

1.3.1 DFT and TD-DFT Calculations

Quantum mechanical density functional theory (DFT) computations reveal that for this compound, the lowest excited states result dominantly from HOMO to LUMO transitions from metal and phosphorus orbitals to dmp ligand orbitals [92] (Figure 1.3). Accordingly, the excited states have significant admixtures of ^{1,3}MLCT character. This assignment is also supported by the photophysical investigations as discussed below. Time-dependent density functional theory (TD-DFT) calculations, carried out in the T_1 state geometry, allow us to estimate an energy separation between the singlet and triplet MLCT states of $\Delta E(S_1–T_1) \approx 0.22$ eV. Since TD-DFT computations give energies of vertical transitions between Franck–Condon states, the calculated $\Delta E(S_1–T_1)$ value is overestimated as demonstrated experimentally (see below) but allows us to expect an occurrence of TADF at ambient temperature.

1.3.2 Flattening Distortions and Nonradiative Decay

An MLCT transition in Cu(I) complexes often leads to flattening distortions of the molecule in the excited state relative to the ground state geometry [114, 116–122, 154, 155]. Such distortions are usually connected with an increase of non-radiative deactivations or even quenching of the emission due to a strong increase of the Franck–Condon factors of the low-lying vibrational modes of the excited state and the highly excited vibrational modes of the electronic ground state [124–126]. Thus, engineering of a highly emissive compound requires that such geometry changes are minimized. This can be achieved by using matrix materials characterized by cages of rigid microenvironments. In a different approach, the excited state distortions can also be reduced or even largely suppressed at the molecular level.

Cu(dmp)(phanephos)$^+$ **21** represents an example of a Cu(I) complex in which the excited state distortions are hindered owing to a rational molecular design. In particular, the diphosphine phanephos with a wide P–Cu–P bite angle of 116° [92] forms a rigid "semicage" for the metal ion coordinated by the second ligand (Figure 1.4). Methyl groups in the 2- and 9-positions of dmp exert steric demands that further hinder flattening distortions. Thus, mutual steric interactions of the chelating ligands strongly reduce flattening distortions and as a consequence radiationless relaxations.

Indeed, Cu(dmp)(phanephos)$^+$ **21** displays intense green-yellow luminescence at ambient temperature even in solution (Figure 1.5). For instance, in dichloromethane (DCM) the quantum yield Φ_{PL} is 40% (Table 1.2). With this Φ_{PL} value and the measured decay time of $\tau(CH_2Cl_2, 300\,K) = 10\,\mu s$, the nonradiative rate k_{nr} can be estimated, using the relation

$$k_{nr} = (1 - \Phi_{PL})/\tau \tag{1.2}$$

The resulting rate of $k_{nr} = 6.0 \times 10^4\ s^{-1}$ represents one of the smallest k_{nr} values found for Cu(I) complexes in liquid solution so far [31]. This proves the validity of the molecular design strategy applied to Cu(dmp)(phanephos)$^+$ **21**. The excited state distortions and, thus, the extent of nonradiative relaxation can further be

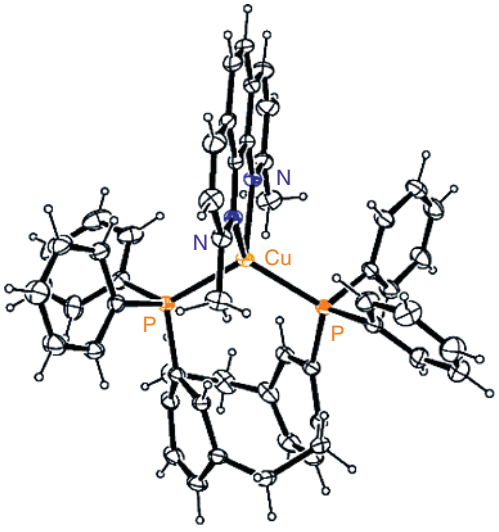

Figure 1.4 Perspective drawing of Cu(dmp)(phanephos)$^+$ **21** (enantiomer *R*) resulting from X-ray crystallography studies. *Source*: Ref. [92]. Adapted with permission of the Royal Society of Chemistry.

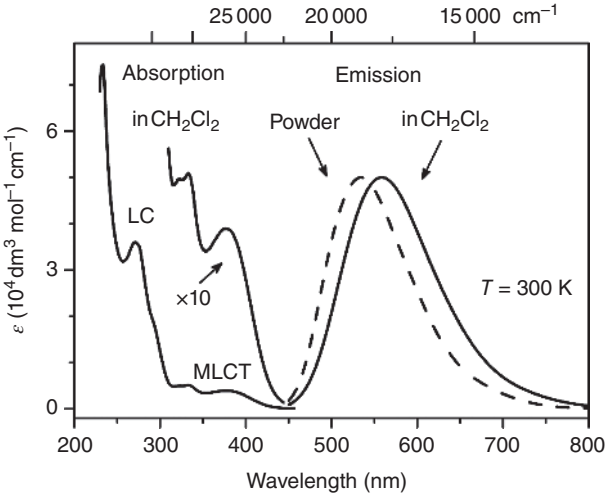

Figure 1.5 Ambient temperature absorption and emission spectra of Cu(dmp)(phanephos)$^+$ **21** recorded in diluted ($c \approx 3 \times 10^{-5}$ M^{-1}) DCM solution (solid lines) and as [Cu(dmp)(phanephos)](PF_6) powder (dashed line). LC and MLCT denote ligand centered (π–π*) and metal-to-ligand charge-transfer (d–π*) transitions, respectively. *Source*: Ref. [92]. Adapted with permission of the Royal Society of Chemistry.

reduced by increasing the rigidity of the environment. Using the Φ_{PL} and τ data summarized in Table 1.2, the rates k_{nr} for a polymer matrix and a solid sample are found to be of $k_{nr} = 1.8 \times 10^4$ s^{-1} (poly(methyl methacrylate), PMMA) and $k_{nr} = 1.4 \times 10^4$ s^{-1} (powder), respectively. Interestingly, the changes of k_{nr} induced by the strongly different matrix rigidities are distinctly less than one order of magnitude. This is regarded as being relatively small, and it indicates that the excited state distortions are already partly suppressed at the level of molecular structure.

Table 1.2 Luminescence properties of [Cu(dmp)(phanephos)](PF_6) **21** in dichloromethane, PMMA (poly(methyl methacrylate)), and as powder.

	$T = 300$ K					$T = 77$ K				
	λ_{max} (nm)	τ (μs)	Φ_{PL} (%)	k_r (s^{-1})	k_{nr} (s^{-1})	λ_{max} (nm)	τ (μs)	Φ_{PL} (%)	k_r (s^{-1})	k_{nr} (s^{-1})
CH_2Cl_2	558	10	40	4.0×10^4	6.0×10^4	548	130	60	4.6×10^3	3.1×10^3
PMMA	535	20	65	3.3×10^4	1.8×10^4	567	170	60	3.5×10^3	2.4×10^3
Powder	530	14	80	5.7×10^4	1.4×10^4	562	240	70	2.9×10^3	1.3×10^3

Source: Ref. [92]. Reproduced with permission of Royal Society of Chemistry.

The discussed trend is also reflected by the small extent of spectral changes observed for the emission spectra. The emission maximum at $T = 300$ K of compound **21** is found at $\lambda_{max} = 558$ nm in DCM. For the compound doped in PMMA, it lies at $\lambda_{max} = 535$ nm and at 530 nm for a powder sample, respectively. Accordingly, the largest blue shift $\Delta\lambda_{max}$ (fluid solution → powder) amounts to $\Delta\lambda(max) = 28$ nm (≈950 cm^{-1}, 118 meV) only. For comparison, for the blue-green emitting Cu(pop)(pz_2BH_2) **25**, $\Delta\lambda(max)$ was found to be as large as 99 nm (≈4200 cm^{-1}) [95]. In the latter case, the large shift is related to the more flexible molecular structure that enables significant flattening distortions in the MLCT excited states. In compound **21**, such distortions are largely suppressed due to the large bite angle and bulky phanephos ligand.

1.3.3 TADF Properties

As expected for a TADF material, the emission decay time τ is strongly dependent on temperature (Table 1.2). Upon heating from $T = 77$ K to ambient temperature, the decay time becomes about one order of magnitude shorter with the quantum yield remaining approximately equally high. Thus, the change of τ is connected to a change of the radiative decay rate k_r. This rate is determined according to the following relation:

$$k_r = \Phi_{PL}/\tau \tag{1.3}$$

In Table 1.2, radiative decay rates are given for different environments and temperatures. In particular, for the powder material k_r amounts to 2.9×10^3 s^{-1} at $T = 77$ K and increases with temperature increase to 5.7×10^4 s^{-1} at ambient temperature, i.e. by a factor of almost 20. Thus, different emission mechanisms are active in the two temperature regimes.

The temperature dependence of the decay time is studied in more detail for a powder sample (Figure 1.6). Between 20 K and about 120 K, the decay time is almost constant and as long as $\tau \approx 240$ μs (plateau). The assignment of this emission to a $T_1 \rightarrow S_0$ phosphorescence is straightforward. Obviously, in this plateau range no other decay mechanism is activated (thermal energy at ≈120 K amounts to ≈83 cm^{-1} or ≈10 meV). However, with further temperature increase, a steep decrease of the decay time is observed, which is due to the

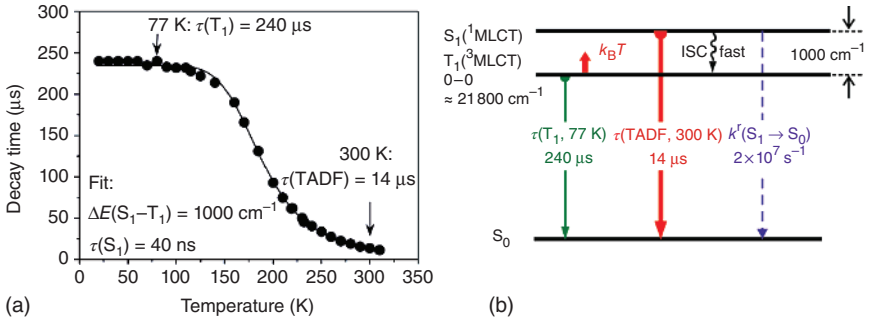

Figure 1.6 (a) Emission decay time of [Cu(dmp)(phanephos)](PF$_6$) **21** powder versus temperature. The emission was excited with a pulsed UV laser at $\lambda_{exc} = 355$ nm (pulse width 7 ns) and detected at $\lambda_{det} = 550$ nm. The solid line represents a fit of Eq. (1.1) to the experimental data fixing the phosphorescence decay time $\tau(T_1) = 240$ µs (plateau at $20\,K < T < 120\,K$). The resulting fit parameters are $\Delta E(S_1–T_1) = 1000\,cm^{-1}$ and $\tau(S_1) = 40$ ns. τ(TADF) = 14 µs is the decay time dominated by the delayed fluorescence at ambient temperature. (b) Energy level diagram for Cu(dmp)(phanephos)$^+$. The radiative rate for the $S_1 \rightarrow S_0$ transition $k_r(S_1 \rightarrow S_0)$ was determined according to Eq. (1.3) assuming $\tau(S_1) = 40$ ns (fit) and $\Phi_{PL} = 80\%$ (measured at ambient temperature). The energy of the $T_1 \rightarrow S_0$ 0–0 transition is estimated from the high-energy flank of the 77 K emission spectrum (not reproduced). *Source*: Ref. [92]. Reproduced with permission of Royal Society of Chemistry.

increase of the radiative decay rate k_r as discussed above. This change is related to a growing involvement of the higher-lying S_1 singlet state with its much higher decay rate of the transition to the electronic ground state S_0. The S_1 state is thermally activated from the lower-lying T_1 state. Hence, the ambient temperature emission represents (largely) a TADF (see also below). It exhibits a decay time of $\tau(\text{TADF}) = 14$ µs at 300 K.

The temperature dependence of $\tau = \tau(T)$, as displayed in Figure 1.6a, can be interpreted in terms of a three states kinetic model involving the electronic ground state S_0, the lowest triplet state T_1, and the lowest excited singlet state S_1, as expressed by Eq. (1.1). By fitting this equation to the measured decay times and inserting the measured decay time $\tau(T_1) = 240$ µs (plateau at $20\,K < T < 120\,K$), values of $\tau(S_1) = 40$ ns and $\Delta E(S_1–T_1) = 1000\,cm^{-1}$ are obtained. The value of $\Delta E(S_1–T_1) = 1000\,cm^{-1}$ corresponds well to the spectral blue shift of $1070\,cm^{-1}$ observed for the emission maximum with temperature increase from $T = 77$ K ($\lambda_{max} = 562$ nm) to 300 K ($\lambda_{max} = 530$ nm) (Table 1.2). This correspondence between the activation energy and the spectral shift upon temperature increase represents a further support for the assignment of the ambient temperature emission as TADF.

For completeness, it is remarked that the emission at ambient temperature frequently does not only represent TADF but also contains some $T_1 \rightarrow S_0$ (phosphorescence) contribution. (Prompt fluorescence is not observed due to fast ISC of the order of a few tens of picoseconds [118, 122, 133, 134, 154, 156–158].) According to Refs [33, 97], the intensity ratio $(S_1)I(T_1)$ can be expressed by

$$\frac{I(S_1)}{I(T_1)} = \frac{k_r(S_1)}{k_r(I) + k_r(II) + k_r(III)} \cdot e^{-\frac{\Delta E(S_1-T_1)}{k_B T}} \tag{1.4a}$$

with

$$k_r(T_1) = \frac{1}{3}(k_r(I) + k_r(II) + k_r(III)) \tag{1.4b}$$

one obtains

$$\frac{I(S_1)}{I(T_1)} = \frac{k_r(S_1)}{3 \cdot k_r(T_1)} \cdot e^{-\frac{\Delta E(S_1 - T_1)}{k_B T}} \tag{1.4c}$$

$k_r(I)$, $k_r(II)$, and $k_r(III)$ are the rates of transitions from the triplet substates I, II, and III of the lowest triplet state (T_1) to the ground state (S_0), respectively. $k_r(T_1) = k_r(T_1 \rightarrow S_0)$ represents the average transition rate from the three triplet substates to the ground state. We will return to the average decay properties later in Section 1.4 (compare Eq. (1.9)). $k_r(S_1) = k_r(S_1 \rightarrow S_0)$ is the transition rate from the lowest excited singlet state (S_1) to the ground state, and $\Delta E(S_1 T_1)$ is the energy gap between states S_1 and T_1 (compare [31, 33]). For Cu(dmp)(phanephos)$^+$ **21** at $T = 300$ K with $\Delta E(S_1 - T_1) = 1000\ cm^{-1}$ (fit, Figure 1.6b), $k_r(S_1) = 2 \times 10^7\ s^{-1}$ (fit), and $k_r(T_1) = 2.9 \times 10^3\ s^{-1}$ (measured at 77 K; Table 1.2), one obtains $I(S_1)/I(T_1) \approx 20$. Thus, the emission spectrum at ambient temperature is clearly dominated by TADF (≈95% TADF, ≈5% phosphorescence from T_1).

1.3.4 Radiative $S_1 \rightarrow S_0$ Rate, Absorption, and Strickler–Berg Relation

The radiative rate $k_r(S_1)$ for the electronic transition between the excited singlet state S_1 and the ground state S_0 can be determined independently from an analysis of the absorption spectrum [92]. According to Figure 1.7, the absorption

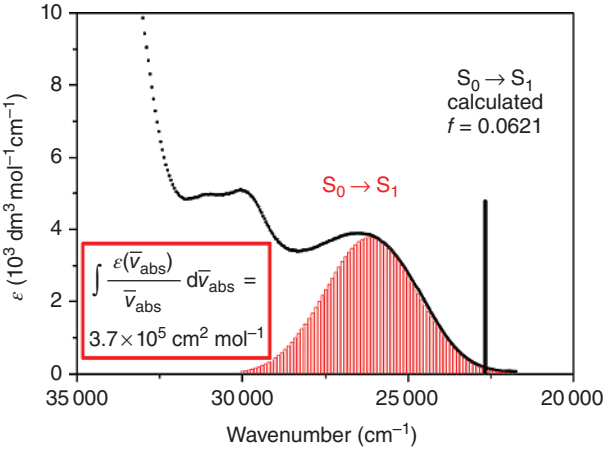

Figure 1.7 Absorption spectrum of Cu(dmp)(phanephos)$^+$ **21** in CH_2Cl_2 at ambient temperature. (Compare Figure 1.5.) The red-shaded area approximates the lowest absorption. The integrated intensity is determined to $3.7 \times 10^5\ cm^2\ mol^{-1}$. The vertical line at $\bar{\nu} = 22\,670\ cm^{-1}$ represents the calculated energy of the $S_0 \rightarrow S_1$ MLCT transition with a relatively small oscillator strength of $f = 0.0621$. The TD-DFT calculation was performed for the ground state optimized geometry at the B3LYP/def2-SVP level of theory. *Source*: Ref. [92]. Adapted with permission of Royal Society of Chemistry.

peak of lowest energy centered at ≈26 300 cm^{-1} (380 nm) and showing a slight spectral overlap with the emission is assigned to the $S_0 \rightarrow S_1$ transition. Thus, a (radiative) transition rate for the related emission $S_1 \rightarrow S_0$ can be estimated using the well-known Strickler–Berg relation between the radiative decay rate of the spontaneous emission and the strength of the corresponding absorption [159]. Accordingly, $k_r(S_1)$ can be expressed as

$$k_r(S_1 \rightarrow S_0) = 8 \cdot \ln 10 \cdot \pi \cdot c \cdot n^2 \cdot N_A^{-1} \cdot \langle \bar{\nu}_{fl}^{-3} \rangle^{-1} \cdot \int \frac{\varepsilon(\bar{\nu}_{abs})}{\bar{\nu}_{abs}} d\bar{\nu}_{abs} \tag{1.5}$$

where c is the speed of light in vacuum, N_A is the Avogadro number, and n is the refractive index of the medium. $\langle \bar{\nu}_{fl}^{-3} \rangle_{av}^{-1}$ displays the reciprocal of the mean value of the third power of the fluorescence energy $\bar{\nu}_{fl}$ (cm^{-1}) (weighted with the emission intensity at each $\bar{\nu}_{fl}$ value of the spectrum). The integral $\int \frac{\varepsilon(\bar{\nu}_{abs})}{\bar{\nu}_{abs}} d\bar{\nu}_{abs}$ represents the absorption strength of the $S_0 \rightarrow S_1$ band. $\varepsilon(\bar{\nu}_{abs})$ is the molar absorption (extinction) coefficient at a given energy $\bar{\nu}_{abs}$. If $\langle \bar{\nu}_{fl}^{-3} \rangle_{av}^{-1}$ is approximated by the third power of the emission maximum $\bar{\nu}_{max}^3$, Eq. (1.5) can be rewritten as

$$k_r(S_1 \rightarrow S_0) = \text{const} \cdot n^2 \cdot \bar{\nu}_{max}^3 \cdot \int \frac{\varepsilon(\bar{\nu}_{abs})}{\bar{\nu}_{abs}} d\bar{\nu}_{abs} \tag{1.6}$$

with const ≈ 2.88×10^{-12} s^{-1} mol cm.

From an integration of the lowest energy absorption band estimated by the shaded area as shown in Figure 1.7, a value of $\int \frac{\varepsilon(\bar{\nu}_{abs})}{\bar{\nu}_{abs}} d\bar{\nu}_{abs} = 3.7 \times 10^5$ cm^2 mol^{-1} is obtained. Thus, for $\bar{\nu}_{max} = 17\,500$ cm^{-1} (emission maximum in CH_2Cl_2 at ambient temperature and with $n = 1.42$), a spontaneous fluorescence rate of $k_r(S_1 \rightarrow S_0) \approx 1.2 \times 10^7$ s^{-1} is obtained. With respect to the different approximations made, this value corresponds reasonably well to the fluorescence decay rate of $k_r(S_1 \rightarrow S_0) \approx 2 \times 10^7$ s^{-1} as determined from the temperature dependence of the emission decay time as discussed above (Figure 1.6).

The value of k_r lying in the range of $1–2 \times 10^7$ s^{-1} corresponds to a moderately allowed transition, as it is expected for a $S_0 \rightarrow {}^1$MLCT transition. The moderate allowedness of this transition is also reflected in the value of the small oscillator strength resulting from TD-DFT calculations (Figure 1.7). For the optimized singlet ground state geometry at the B3LYP/def2-SVP level of theory, the oscillator strength for the $S_0 \rightarrow S_1$ transition of $f = 0.0621$ is obtained [92]. With a simple relation, the radiative rate can be estimated according to [124]:

$$k_r \cong \bar{\nu}^2 f \tag{1.7}$$

where $\bar{\nu}$ is the energy (in wave numbers) corresponding to the maximum wavelength of absorption. With the calculated value of $f = 0.0621$ and the $S_0 \rightarrow S_1$ transition energy of 22 670 cm^{-1}, a radiative rate of 3×10^7 s^{-1} is estimated, being in agreement with the value of $k_r(S_1 \rightarrow S_0) = 2 \times 10^7$ s^{-1} as determined experimentally.

With respect to the approximations made applying the different and independent methods, the $k_r(S_1 \rightarrow S_0)$ values (2×10^7 s^{-1} from the decay time analysis, 1.2×10^7 s^{-1} from the absorption strength analysis, and 3×10^7 s^{-1} from a

TD-DFT approach) are in good agreement. This is an important result, since it strongly supports the TADF assignment with respect to the involvement of the singlet S_1 state in the emission process at ambient temperature. Moreover, it is concluded that the geometry changes that still take place upon excitation do not significantly alter the $S_1 \rightarrow S_0$ transition rate determined for the relaxed geometry (from emission properties) as compared with the rate determined for the unrelaxed molecular geometry (from absorption).

1.4 Case Study: TADF of a Cu(I) Complex with Small $\Delta E(S_1–T_1)$

As already addressed, Cu(I) complexes display a large variety of TADF properties. In particular, this is related to a large range of energy separations $\Delta E(S_1–T_1)$ between the lowest singlet and triplet state being larger than 10^3 cm^{-1} (120 meV) or as small as a few hundred cm^{-1}. In Section 1.3, a complex with a relatively large $\Delta E(S_1–T_1)$ was presented. In the present case study, we will focus on a complex characterized by a small $\Delta E(S_1–T_1)$ value and discuss related TADF properties.

1.4.1 DFT and TD-DFT Calculations

In Figure 1.8, frontier orbital plots of Cu(dppb)(pz_2Bph_2) **2** (with dppb = 1,2-bis(diphenylphosphino)benzene and pz_2Bph_2 = diphenylbis(pyrazolylborate)) are reproduced together with the complex' chemical structure. The HOMO is derived from a metal 3d atomic orbital with significant contributions from the coordinating phosphorus and nitrogen atoms, whereas the LUMO is localized on the *o*-phenylene ring of the dppb ligand. Thus, similarly to Cu(dmp)(phanephos)$^+$ **21**, the orbitals display distinctly different spatial distributions, and the related HOMO → LUMO excitations are of CT character. It can be further shown by

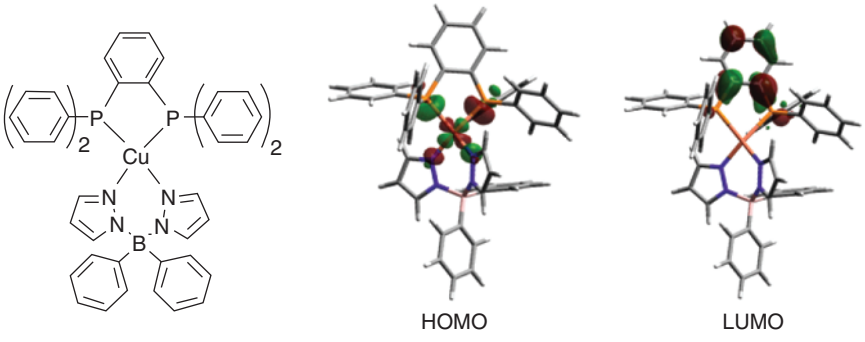

Figure 1.8 Chemical formula and contour plots of the HOMO and LUMO of Cu(dppb)(pz_2Bph_2) **2** resulting from DFT calculations for the triplet state geometry at the B3LYP/def2-SVP level of theory. The frontier orbitals exhibit distinctly different spatial distributions. The HOMO is mainly composed of the copper 3d and phosphorus sp^3 atomic orbitals, while the LUMO represents a π^* orbital of the dppb ligand. Compare [96].

TD-DFT calculations that the lowest excited singlet state S_1 and the triplet state T_1 are of more than 90% of HOMO–LUMO character [96]. Due to the distinct involvement of the metal, these states are assigned to largely represent ^{1}MLCT and ^{3}MLCT states, respectively. The significant spatial separation of HOMO and LUMO allows us to predict a relatively small exchange interaction and, thus, a small singlet–triplet energy separation $\Delta E(S_1-T_1)$. Indeed, TD-DFT calculations in the triplet state optimized geometry give a small value of $\Delta E(S_1-T_1) = 72$ meV ($\approx$580 cm^{-1}), estimated as the energy difference between vertical $S_0 \rightarrow S_1$ and $S_0 \rightarrow T_1$ transitions [96] (Table 1.3), as being three times smaller than the value calculated for Cu(dmp)(phanephos)$^+$ **21**. Again, the $\Delta E(S_1-T_1)$ value calculated as the energy difference between the computed vertical excitations is overestimated. The experimentally determined activation energy amounts to $\Delta E(S_1-T_1) = 370$ cm^{-1} (46 meV).

According to the spatial separation of the molecular orbitals involved in the transition between the electronic ground state S_0 and the lowest excited singlet state S_1 (^{1}MLCT), it can be predicted that the transition dipole moment and, thus, the oscillator strength of the transition is relatively small. Indeed, TD-DFT calculations performed for the T_1 geometry at the B3LYP/def2-SVP level of theory result to $f = 0.0016$, being more than one order of magnitude smaller than the value 0.0201 calculated for the $S_0 \rightarrow S_1$ transition of complex [Cu(dmp)(phanephos)]$^+$ **21**. Further results of TD-DFT calculations are presented in Table 1.3 that are later used to explain effects of SOC in complex **2**.

1.4.2 Emission Spectra and Quantum Yields

Emission properties of Cu(dppb)(pz_2Bph_2) **2** were studied for powder samples over a wide temperature range from $T = 1.5$ to 300 K. Figure 1.9 displays representative emission spectra. Emission maxima, quantum yields, and decay times are collected in Table 1.4.

The compound shows intense green-yellow luminescence at all temperatures in the investigated range of 1.5–300 K, with quantum yields Φ_{PL} of 70% at ambient temperature and about 100% at $T = 77$ K. The spectra are broad and unstructured, which correlates with the predicted MLCT character of the corresponding electronic transitions. With temperature increase to $T \geq 30$ K, only a small blue shift is observed with the emission maximum λ(max) shifting from 548 nm at 1.5 K (not shown) and 30 K to 535 nm at 80 and 300 K. This is a consequence of the thermal activation of the TADF decay path via the higher-lying S_1 state above $T \approx 50$ K (see below).

1.4.3 The Triplet State T_1 and Spin–Orbit Coupling

The emission spectra do not display distinct changes with temperature change. However, the decay kinetics varies drastically even at very low temperature (below $T = 20$ K). This is related to the properties of the triplet state and its substates. Therefore, before discussing effects of thermal activation of the singlet state, the TADF effect, we want to focus on triplet state properties.

Table 1.3 Vertical transition energies, oscillator strengths, and main orbital contributions of selected electronic transitions of Cu(dppb)(pz_2Bph_2) **2** resulting from TD-DFT calculations for the optimized triplet state geometry (T_1 state) at the B3LYP/def2-SVP level of theory.

Transition	Energy (eV)	Oscillator strength	Main contribution
$S_0 \rightarrow T_1$	1.303	0	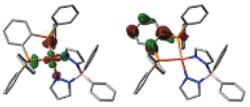 HOMO → LUMO
$S_0 \rightarrow T_2$	1.926	0	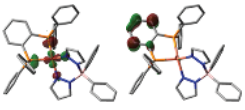 HOMO → LUMO + 1
$S_0 \rightarrow T_3$	2.404	0	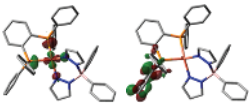 HOMO → LUMO + 2
$S_0 \rightarrow T_4$	2.601	0	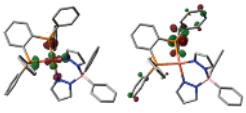 HOMO → LUMO + 3
$S_0 \rightarrow T_5$	2.681	0	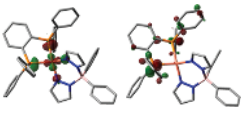 HOMO → LUMO + 4
$S_0 \rightarrow S_1$	1.375	0.0016	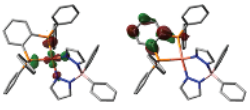 HOMO → LUMO
$S_0 \rightarrow S_2$	2.033	0.0038	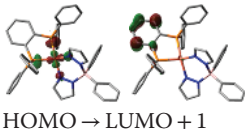 HOMO → LUMO + 1
$S_0 \rightarrow S_3$	2.623	0.0547	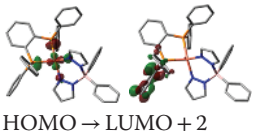 HOMO → LUMO + 2
$S_0 \rightarrow S_4$	2.746	0.0253	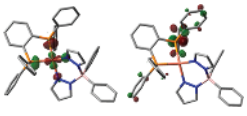 HOMO → LUMO + 3

Table 1.3 (Continued)

Transition	Energy (eV)	Oscillator strength	Main contribution
$S_0 \rightarrow S_5$	2.814	0.0727	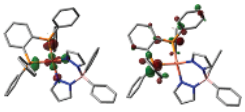 HOMO → LUMO + 4
$S_0 \rightarrow S_6$ SOC[a)]	2.848	0.0102	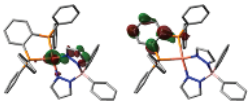 HOMO−1 → LUMO

The lowest $S_0 \rightarrow S_n$ transition of HOMO−n → LUMO character that contains different Cu-3d character than the HOMO and that can exhibit SOC to the T_1 state is marked (see text).
a) SOC to T_1 possible.
Source: Refs [31, 96]. Reproduced with permission of Elsevier.

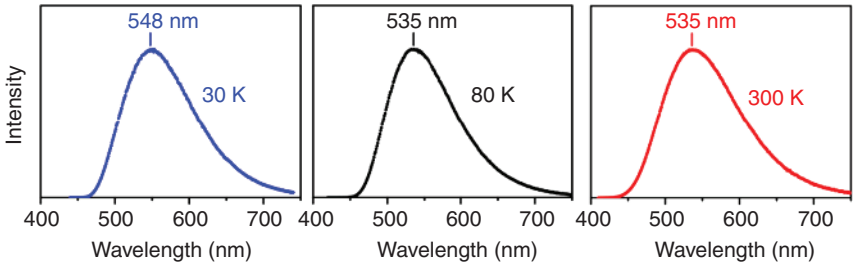

Figure 1.9 Luminescence spectra of Cu(dppb)(pz_2Bph_2) **2** powder recorded at different temperatures. *Source*: Ref. [96]. Reproduced with permission of American Chemical Society.

Table 1.4 Emission data for a powder sample of Cu(dppb)(pz_2Bph_2) **2**.

Temperature (K)	λ_{max} (nm)	Φ_{PL} (%)	τ (μs)	k_r (s^{-1})[a)]	k_{nr} (s^{-1})[a)]
300	535	70	3.3	210×10^3	9×10^4
80	535	≈100[b)]	300	3.3×10^3	—
30	548	≈100[b)]	1200	8.3×10^2	—

a) k_r and k_{nr} are determined by the use of Eqs. (1.2) and (1.3), respectively.
b) It is assumed that the quantum yield Φ_{PL} at $T = 30$ K amounts to 100%, as determined experimentally at $T = 77$ K.
Source: Ref. [96]. Reproduced with permission of American Chemical Society.

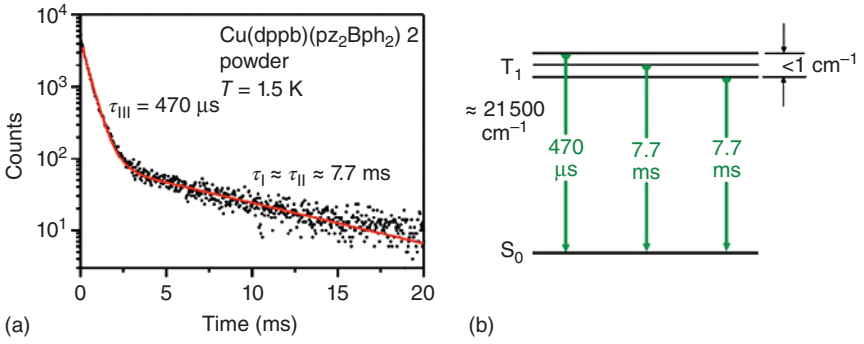

Figure 1.10 (a) Emission decay curve of Cu(dppb)(pz_2Bph_2) **2** at 1.5 K recorded for a powder sample after pulsed excitation at $\lambda_{exc} = 372$ nm and with signal detection at $\lambda_{det} = 550$ nm. *Source*: Ref. [96]. Reproduced with permission of American Chemical Society. (b) Energy level scheme showing the triplet substates and the related decay paths at $T = 1.5$ K at vanishing fast equilibration.

At $T = 1.5$ K, the decay curve is distinctly nonmonoexponential. The decay curve can be fitted with a bi-exponential function with the time constants of 7.7 ms and 470 µs (Figure 1.10). These different decay constants are assigned to emissions from the three individual triplet T_1 substates I, II, and III with $\tau_I \approx \tau_{II} = 7.7$ ms and $\tau_{III} = 470$ µs, respectively. It is remarked that for Cu(I) complexes, frequently a bi-exponential decay behavior is observed and not a tri-exponential one as expected for three triplet substates [57, 88, 160, 161]. This is due to the fact that the decay times of two substates are often very similar [33, 95–97]. Theoretical calculations based on SOC-TD-DFT (ADF2014) computations support this assignment [162].

At low temperature of $T = 1.5$ K, these T_1 substates are not thermally equilibrated due to slow SLR [57, 88, 137, 160, 161]. This behavior is related to small ZFSs of the T_1 state of less than 1 or 2 cm^{-1} (0.1 or 0.2 meV) [9, 57, 70, 88, 160, 161]. Such a small ZFS value is a consequence of weak SOC of the T_1 substates with higher-lying states. Furthermore, the emission decay time of $\tau(T_1) = 1200$ µs (at 30 K) is extremely long if compared with Cu(dmp)(phanephos)$^+$ **21** (Section 1.3) and many other Cu(I) complexes [9, 31, 33, 35, 40, 42, 46, 50, 70, 92, 95–98, 100, 135, 163, 164]. Again, this is a consequence of the weak SOC with respect to the lowest triplet state.

Obviously, the (weak) allowedness of the $T_1 \rightarrow S_0$ transition is not dominantly related to the SOC constant of copper, which is with $\zeta = 857$ cm^{-1} [165] not very small. More important is the extent of mixing of energetically higher-lying singlet state(s). In a very simplified perturbational approach, the radiative rate can be described by [31, 69, 70, 166]:

$$k_r(T_1 \rightarrow S_0) \approx \text{const} \cdot \frac{|\langle S_m|H_{SO}|T_1\rangle|^2}{|E(T_1) - E(S_m)|^2} \cdot |\langle S_0|e\vec{r}|S_m\rangle|^2 \quad (1.8)$$

H_{SO} is the SO operator. $E(S_m)$ and $E(T_1)$ are the (unperturbed) energies of the (pure) singlet state S_m and the (pure) triplet state T_1, respectively. In this simple

model, it is assumed that one higher-lying singlet state S_m couples dominantly to the state T_1, i.e. to at least one T_1 triplet substate. $\langle S_0|\vec{er}|S_m\rangle$ is the dipole matrix element with the dipole operator $\vec{er}$.

A discussion of the energy denominator and its size is particularly helpful. Presumably, SOC with the energetically most proximate singlet state of adequate character represents a leading contribution to the radiative rate. Therefore, Eq. (1.8) shows only one mixing singlet state, being the state S_m, although several other singlet states may additionally contribute to the allowedness of the $T_1 \rightarrow S_0$ transition.

Quantum mechanical considerations show that SOC between a triplet state T_1 and a singlet state S_1 that both stem from the same orbital configuration, for example, from the HOMO → LUMO excitation, is negligible as for efficient SOC different d orbitals must be involved in the coupling states [9, 30, 31, 69–72, 75, 167].

The TD-DFT calculations presented above for compound **2** show that the energetically nearest singlet state that involves another d orbital than the T_1 state is the singlet state S_6. It originates from the HOMO − 1 → LUMO electronic transition. According to Table 1.3, the energy separation that is responsible for dominant SOC amounts to $\Delta E(S_6-T_1) = 1.545\,\text{eV}$ ($\approx 12\,500\,\text{cm}^{-1}$) ($\Delta E(\text{HOMO} - (\text{HOMO}-1)) = 1.4\,\text{eV}$). As a consequence of this large energy denominator (Eq. 1.8), the triplet state does not experience effective SOC with state S_6. Hence, the phosphorescence decay time is expected to be very long. Indeed, this is found for compound **2** with $\tau(T_1 \rightarrow S_0) = 1200\,\mu\text{s}$. For comparison, the phosphorescence decay time of a compound that exhibits a much smaller energy denominator is given. For example, $Cu_2Cl_2(N\text{^}P)_2$ **18** with an energy separation between HOMO and HOMO−1 (that involve different d orbitals) amounts to only 0.378 eV ($3000\,\text{cm}^{-1}$) [31, 97]. Since this HOMO−1 → LUMO excitation essentially defines the S_2 state, the energy separation to the T_1 state is much smaller than for compound **2**. Accordingly, the mixing of S_2 and T_1 becomes distinctly stronger (Eq. 1.8), and, hence, the triplet decay time amounts to only $\tau(T_1 \rightarrow S_0) = 43\,\mu\text{s}$ [31, 97]. Thus, the $T_1 \rightarrow S_0$ allowedness of compound **18** is by a factor of almost 30 higher than found for compound **2**.

The size of the squared dipole matrix element $\langle S_0|\vec{er}|S_m\rangle$ with the dipole operator $\vec{er}$ is also of importance for the radiative rate $k_r(T_1 \rightarrow S_0)$ (or more exactly for the rate of the individual triplet substate that mixes with S_m). The corresponding value is proportional to the oscillator strength or the molar absorption coefficient of the singlet–singlet transition $S_0 \rightarrow S_m$, whereby S_m is the singlet state that can mix with the T_1 state via SOC [69, 72]. With respect to the corresponding allowedness, it is referred to Table 1.3.

For completeness, it is remarked that literature discussions frequently assume dominating SOC between T_1 and S_1. However, for compound **2**, the corresponding energy separation is very small amounting to only $\Delta E(S_1-T_1) = 370\,\text{cm}^{-1}$ (see below). As a consequence, relatively strong SOC would be expected to occur. Above, it has been demonstrated that this is not the case. Obviously, the simple literature approach is not suited.

1.4.4 Temperature Dependence of the Emission Decay Time and TADF

Let us focus on the temperature dependence of the emission decay time. With temperature increase, the SLR processes become faster (presumably according to a Raman process of SLR [137, 138, 160]), resulting in a fast thermalization of the three T_1 substates. At sufficiently high temperature, e.g. above $T = 10$ or 20 K, an average emission decay time τ_{av} is normally observed as expressed by Eq. (1.9) [9, 33, 57, 70, 88, 95, 96, 137, 139, 161]:

$$\tau_{av} = 3(\tau_I{}^{-1} + \tau_{II}{}^{-1} + \tau_{III}{}^{-1})^{-1} \tag{1.9}$$

Inserting the decay times of $\tau_I \approx \tau_{II} = 7.7$ ms and $\tau_{III} = 470$ µs, as determined at $T = 1.5$ K, one obtains $\tau_{av} = 1250$ µs. Almost the same value of $\tau(T_1) = 1200$ µs (monoexponential decay) is measured at $T = 30$ K (Figure 1.11). Thus, the assignments of the decay times we made above are validated.

Figure 1.11 displays emission decay curves and the temperature dependence of the decay time for the range of 20 K ≤ T ≤ 300 K. From $T = 20$ K to about 40 K, the decay time remains constant (plateau) with $\tau(T_1) = 1200$ µs. With further temperature increase, the decay time decreases drastically to $\tau(80\,K) = 300$ µs and $\tau(300\,K) = 3.3$ µs. The plot of the measured τ values versus temperature has a characteristic form of an s-shaped curve similar to the one obtained for Cu(dmp)(phanephos)$^+$ **21** (Figure 1.6a) but with the point of maximum slope shifted from 180 to 70 K for compound **2**. The radiative rate k_r, determined by the use of Eq. (1.3), rises from the low-temperature value of $k_r(30\,K) = 8.3 \times 10^2$ s^{-1} to $k_r(80\,K) = 3.3 \times 10^3$ s^{-1}, and to $k_r(300\,K) = 2.1 \times 10^5$ s^{-1}, respectively (Table 1.4). The latter value represents a rate increase by a factor of 250 as compared with the $k_r(30\,K)$ value. This drastic increase of the radiative rate combined with the spectral blue shift of 13 nm with temperature increase (Figure 1.9) is explained by an involvement of a higher-lying state that carries a higher radiative rate, hence demonstrating the occurrence of TADF.

An analysis of the decay time data according to the Boltzmann-type Eq. (1.1) leads to an activation energy of $\Delta E(S_1–T_1) = 370$ cm^{-1} and a prompt fluorescence decay rate of $k_r(S_1 \rightarrow S_0) = 3.9 \times 10^6$ s^{-1} (taking the emission quantum yield of $\Phi_{PL} = 70\%$ as measured at 300 K into account) (Figure 1.11).[1] Again, it is stressed that the prompt fluorescence could not be observed directly in our experiments conducted with nanosecond time resolution. This agrees with measured ISC time of the order of several picoseconds [118, 122, 134, 154, 156–158]. The resulting energy level diagram and the relevant rates are summarized in Figure 1.11c.

The value of $\Delta E(S_1–T_1) = 370$ cm^{-1} represents one of the smallest splitting values found so far [31, 96]. Accordingly, Cu(dppb)(pz_2Bph_2) **2** shows a very short

1 For completeness, it is remarked that the value of $k^r(S_1 \rightarrow S_0) = 3.9 \times 10^6$ s^{-1} represents a coarse estimate, since Eq. (1.1) is only valid, if the parameters in this equation, $k(T_1)$, $k(S_1)$, and $\Delta E(S_1–T_1)$, are independent of temperature. This is not strictly the case, since the emission quantum yield decreases with temperature. However, an alternative fit can be applied when we restrict the temperature range for the fit procedure to 30 ≤ T ≤ 150 K. Then it is reasonable to assume constant parameters, in particular, the emission quantum yield should be almost constant, i.e. ≈100% as measured at $T = 80$ K [96]. For this restricted fit range, essentially the same fit parameters are obtained as discussed above. For this situation, we find $\tau(S_1) = 180$ ns at $\Phi_{PL} = 100\%$ and a rate of $k^r(S_1) = 5.6 \times 10^6$ s^{-1}.

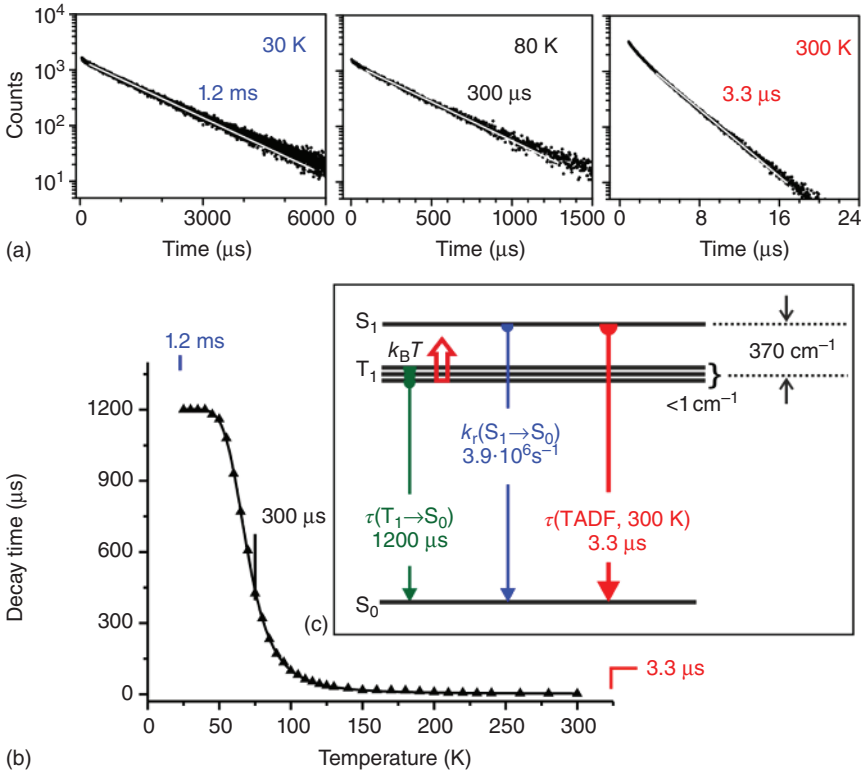

Figure 1.11 (a) Emission decay profiles of Cu(dppb)(pz_2Bph_2) **2** (powder) at 30, 80, and 300 K recorded after pulsed excitation at $\lambda_{exc} = 378$ nm and detected at $\lambda_{det} = 540$ nm. (b) Emission decay time τ versus temperature. The solid line represents a fit of Eq. (1.1) to the experimental $\tau(T)$ values fixing $\tau(T_1) = 1.2$ ms as measured at $T = 30$ K. The fit parameters are $\tau(S_1) = 180$ ns and $\Delta E(S_1–T_1) = 370$ cm^{-1}, respectively. (c) Energy level diagram of Cu(dppb)(pz_2Bph_2) **2**. Both competing emission processes are marked: Phosphorescence with a decay time of $\tau(T_1) = 1.2$ ms dominating the photophysical behavior at temperatures below about 50 K and TADF determining the emission properties at higher temperatures with a measured decay time at 300 K of 3.3 µs (with the emission quantum yield of $\Phi_{PL} = 70\%$). *Source*: Ref. [96]. Reproduced with permission of American Chemical Society.

TADF decay time of $\tau(\text{TADF}) = 3.3$ µs, being one of the shortest values reported so far for Cu(I) complexes (compare Section 1.6).

The experimental characterization of the luminescence behavior of Cu(dppb)(pz_2Bph_2) **2** supports the predictions based on model calculations, as developed above. According to the distinct spatial separation of the orbitals involved in the lowest excited states, the (formal) fluorescence decay time of $\tau(S_1) = 180$ ns (calculated from $k_r(S_1 \rightarrow S_0) = 3.9 \times 10^6$ s^{-1} and $\Phi_{PL} = 70\%$) is relatively long for a spin-allowed transition. For instance, it is about four times longer than the decay time of the S_1 state as determined for Cu(dmp)(phanephos)$^+$ **21** (Section 1.3). A large difference of the $\tau(S_1)$ lifetimes could be predicted by the TD-DFT calculations, as the oscillator strength of the corresponding $S_0 \rightarrow S_1$ transition (calculated for the T_1 state geometry), being 0.0016 for

Cu(dppb)(pz_2Bph_2) **2** (Table 1.3), is more than an order of magnitude smaller than calculated for Cu(dmp)(phanephos)$^+$ **21** with $f = 0.0201$ (Section 1.3).

Interestingly, the case studies presented in Sections 1.3 and 1.4 focusing on two complexes with very different allowedness of the $S_1 \leftrightarrow S_0$ transitions is displayed inversely in the size of the energy splitting $\Delta E(S_1–T_1)$. For Cu(dmp)(phanephos)$^+$ **21**, it amounts to 1000 cm^{-1} (120 meV), while for Cu(dppb)(pz_2Bph_2) **2** a value of 370 cm^{-1} (46 meV) is found. This important relation will be addressed in Section 1.5.

Moreover, the photophysical studies presented in Sections 1.3 and 1.4 reveal an important practical conclusion concerning the assignments of emission processes. Both compounds show a phosphorescence plateau at low temperatures, at $T < 120$ K in the case of Cu(dmp)(phanephos)$^+$ **21** with $\Delta E(S_1–T_1) = 1000\ cm^{-1}$ and at $T < 50$ K in the case of Cu(dppb)(pz_2Bph_2) **2** with $\Delta E(S_1–T_1) = 370\ cm^{-1}$, respectively. At ambient temperature, the emission of both compounds represents TADF. Importantly, in many laboratories only two temperature regimes of $T = 300$ K (ambient temperature) and $T = 77$ K (boiling point of nitrogen) are easily accessible. Therefore, characterization of new compounds is usually performed at these two temperatures. Based on these results, preliminary conclusions concerning the character of the emissive states and the emission mechanism(s) are drawn. For Cu(dmp)(phanephos)$^+$ **21**, with the measured decay time of $\tau(77\ K) = 240$ µs (plateau range between 20 and 120 K) and $\tau(300\ K) = 14$ µs, respectively, the emissions at low temperature and at ambient temperature would be assigned correctly as phosphorescence from the T_1 state and as TADF, respectively. For Cu(dppb)(pz_2Bph_2) **2** with $\tau(77\ K) = 300$ µs and $\tau(300\ K) = 3.3$ µs, a similar assignment would not be correct. As shown in Figure 1.11, the phosphorescence decay time $\tau(T_1) = 1200$ µs (plateau for $T \leq 40$ K) is four times longer than found at 77 K. Thus, the emission at 77 K cannot be assigned as phosphorescence. On the contrary, it represents mainly delayed fluorescence (TADF) even at $T = 77$ K. The ratio of TADF to phosphorescence is estimated (by the use of Eq. (1.4c)) to 75% : 25%. Correspondingly, the emission spectra recorded at $T = 77$ K and 300 K are not shifted with respect to each other as for the two temperatures, the spectral maxima of compound **2** are found at 535 nm. Thus, conclusions made on the basis of 77 K and ambient temperature measurements must be taken with care. The risk of possible misinterpretation is particularly large when the energy separation $\Delta E(S_1–T_1)$ is small.

1.5 Energy Separation $\Delta E(S_1–T_1)$ and $S_1 \rightarrow S_0$ Fluorescence Rate

In Section 1.2, it was already shortly discussed that a reduction of the energy separation between the lowest singlet S_1 and triplet T_1 state is connected with a decrease of the radiative singlet–singlet rate $k_r(S_1 \rightarrow S_0)$. This relation has also been addressed in the two previous sections based on case studies. Since both photophysical parameters crucially determine the TADF behavior, in particular, the TADF decay time, we want to focus in this section on a simple model that may explain this relation.

1.5.1 Experimental Correlation Between $\Delta E(S_1–T_1)$ and $k_r(S_1 \rightarrow S_0)$ for Cu(I) Compounds

During the last years, the $\Delta E(S_1–T_1)$ energy separations and the $S_1 \rightarrow S_0$ fluorescence decay times have been determined for a large number of Cu(I) compounds that show TADF. Both parameters result from fit procedures by the use of Eq. (1.1). For two compounds, this has been discussed in detail in Sections 1.3 and 1.4. It is stressed again that the prompt fluorescence was not observed directly, but the corresponding $k_r(S_1 \rightarrow S_0)$ rate could be determined. In Table 1.5, adapted from Ref. [31], we summarize the corresponding data for Cu(I) compounds. The fitting procedure leads to the formal (prompt) decay time $\tau(S_1)$ or to the rate $k(S_1 \rightarrow S_0)$. From this information and by the use of the measured photoluminescence quantum yield (Φ_{PL}), one can easily determine the radiative rate $k_r(S_1 \rightarrow S_0)$ applying Eq. (1.3).

In Figure 1.12, the $k_r(S_1 \rightarrow S_0)$ data are plotted versus $\Delta E(S_1–T_1)$. It is obvious that with decreasing energy splitting, the allowedness of the $S_1 \rightarrow S_0$ transition decreases drastically. For example, if compound **25** is compared with compound **1**, $\Delta E(S_1–T_1)$ decreases from 1300 to 270 cm^{-1}, while the allowedness of the

Table 1.5 Energy separation $\Delta E(S_1–T_1)$ and radiative rate $k_r(S_1 \rightarrow S_0)$ determined by fitting procedures applying Eq. (1.1) to experimental decay time data. $\tau(S_1)$ is the (formal) prompt fluorescence decay time and Φ_{PL} the emission quantum yield.

	Compound	$\Delta E(S_1–T_1)$ (cm^{-1})	$\tau(S_1)$ (ns)	Φ_{PL} (300 K)	$k_r(S_1 \rightarrow S_0)$ ($10^6 \times s^{-1}$)	References
1	Cu_2I_2[MePyrPHOS]$(Pph_3)_2$	270	570	0.97	1.7	[30]
2	Cu(dppb)(pz_2Bph_2)	370	180	0.70	3.9	[96]
3	$[Cu(\mu\text{-Cl})(PNMe_2)]_2$	460	210	0.45	2.1	[33]
4	$[Cu(\mu\text{-Br})(PNMe_2)]_2$	510	110	0.65	5.9	[33]
5	$[Cu(\mu\text{-I})(PNMe_2)]_2$	570	90	0.65	7.2	[33]
6	$Cu_2Cl_2(dppb)_2$	600	70	0.35	5.0	[107]
7	$[Cu(\mu\text{-I})(PNpy)]_2$	630	100	0.65	6.5	[33]
8	Cu(pop)(pz_2BPh_2)	650	170	0.9	5.3	[9, 95]
14	$Cu(tmbpy)(pop)^+$	720	160	0.55	3.4	[35]
15	$(IPr)Cu(py_2\text{-}BMe_2)$	740	160	0.76	4.8	[34]
16	$[Cu(PNP^tBu)]_2$	786	79	0.57	7.2	[46]
17	Cu_2I_2(MePyrPHOS)(dpph)	830	190	0.88	4.6	[30]
18	$Cu_2Cl_2(N\text{^}P)_2$	930	40	0.92	23	[97]
19	$CuCl(Pph_3)_2$(4-Mepy)	940	47	0.99	21	[98]
21	$Cu(dmp)(phanephos)^+$	1000	40	0.80	20	[92]
22	Cu(pop)(pz_4B)	1000	80	0.9	11	[95]
23	$CuBr(Pph_3)_2$(4-Mepy)	1070	41	0.95	23	[98]
24	$CuI(Pph_3)_2$(4-Mepy)	1170	14	0.66	47	[98]
25	Cu(pop)(pz_2BH_2)	1300	10	0.45	45	[70, 95]

Source: Ref. [31]. Adapted with permission of Elsevier.

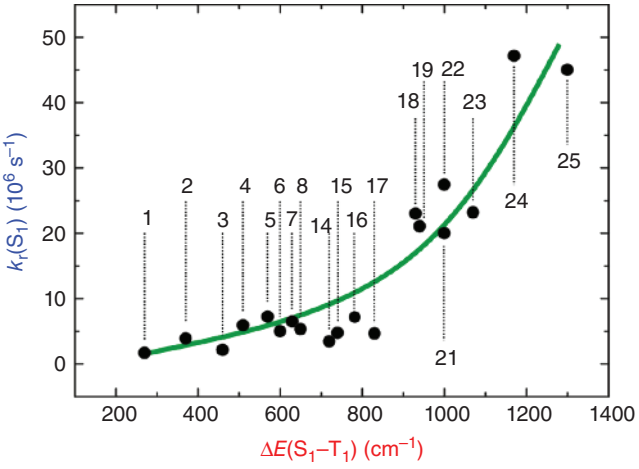

Figure 1.12 Radiative decay rate $k_r(S_1–S_0)$ plotted versus $\Delta E(S_1–T_1)$ for different Cu(I) complexes that show TADF at ambient temperature (data from Table 1.5). The fit curve represents an exponential function as guide for the eye. *Source*: Ref. [31]. Reproduced with permission of Elsevier.

$S_1 \rightarrow S_0$ transition decreases by a factor of about 26. In a simple consideration, using Eq. (1.1), it can be seen that the TADF decay time will not become shorter, when $\Delta E(S_1–T_1)$ reaches 300 to 200 cm^{-1} (≈40 or 25 meV). Such a minimum decay time lies in the range of several microsecond [168], at least for the type of Cu(I) compounds discussed here.

1.5.2 Quantum Mechanical Considerations

In this section, we want to illustrate on a simple quantum mechanical basis, following [31], why a small energy separation $\Delta E(S_1–T_1)$ between the lowest singlet S_1 and triplet T_1 state is related to a fast radiative rate of the $S_1 \rightarrow S_0$ transition, i.e. a small $k_r(S_1 \rightarrow S_0)$ value. Let us assume that S_1 and T_1 can be described by a one-electron transition from HOMO φ_H to LUMO φ_L. In this situation, simple expressions can be given for the radiative rate $k_r(S_1–S_0)$ $(= k_r(S_1 \rightarrow S_0))$ and the energy splitting $\Delta E(S_1–T_1)$.

The radiative rate may be obtained from the transition dipole moment $\vec{\mu}(S_1 - S_0)$, which is approximately given by

$$\vec{\mu}_{H,L} = e \int \varphi_H(\vec{r})\vec{r}\varphi_L(\vec{r})d^3r = e \int \varphi_H(\vec{r})\varphi_L(\vec{r})\vec{r}\ d^3r \tag{1.10}$$

$\vec{r}$ is the dipole vector and e is the electron charge.

Thus, the radiative rate can be expressed by (see Ref. [169], p. 159), [31]:

$$k_r(S_1 - S_0) = 2Cv^3n^3|\vec{\mu}_{HL}|^2 \tag{1.11}$$

$$k_r(S_1 - S_0) = 2e^2Cv^3n^3\left|\int \varphi_H(\vec{r})\varphi_L(\vec{r})\vec{r}\ d^3r\right|^2 \tag{1.12}$$

with the numerical constant $C = 16\pi^3/(3\varepsilon_0 hc^3)$, wherein ε_0 is the vacuum permittivity, h is Planck's constant, and c is the velocity of light. $\nu = \Delta E(S_1–S_0)/h$ is the transition frequency and n the refractive index.

The energy separation $\Delta E(S_1–T_1)$ can be expressed in this approximation by twice the exchange integral K_{HL} for HOMO and LUMO (see Ref. [[130], p. 86]) giving

$$\Delta E(S_1 - T_1) \approx 2K_{HL} \tag{1.13}$$

with

$$K_{HL} = \frac{e^2}{4\pi\varepsilon_0} \int \varphi_H(\vec{r}_1)\varphi_L(\vec{r}_2)\frac{1}{|\vec{r}_2 - \vec{r}_1|}\varphi_H(\vec{r}_2)\varphi_L(\vec{r}_1)\mathrm{d}^3 r_1 \ \ \mathrm{d}^3 r_2 \tag{1.14}$$

or

$$K_{HL} = \frac{e^2}{4\pi\varepsilon_0} \int \varphi_H(\vec{r}_1)\varphi_L(\vec{r}_1)\frac{1}{|\vec{r}_2 - \vec{r}_1|}\varphi_H(\vec{r}_2)\varphi_L(\vec{r}_2)\mathrm{d}^3 r_1 \ \ \mathrm{d}^3 r_2 \tag{1.15}$$

It is an important result that both the exchange interaction and hence the energy splitting $\Delta E(S_1–T_1)$ (Eq. (1.13)) as well as the radiative rate (Eq. (1.12)) depend quadratically on the product of $\varphi_H(r)\varphi_L(r)$ or the squared overlap of HOMO and LUMO.[2] Accordingly, it becomes obvious that $\Delta E(S_1–T_1)$ and $k_r(S_1 \rightarrow S_0)$ correlate. A small HOMO–LUMO overlap implies small $\Delta E(S_1–T_1)$ and small $k_r(S_1 \rightarrow S_0)$. This relation is schematically illustrated in Figure 1.13.

The simple qualitative model presented above allows us to understand the experimental results as displayed in Figure 1.12. The model's basic assumption is that the low-lying singlet S_1 and triplet T_1 states, originating from the HOMO → LUMO excitation, are energetically well separated from higher-lying energy states. Accordingly, in the scope of this material class (or this model), we cannot reduce the TADF decay time distinctly below a few microsecond. However, the simple model, being valid for the compounds shown in Table 1.5, does not contain mixing of the singlet state S_1 with a higher-lying singlet state that carries high oscillator strength with respect to the transition to the electronic ground state. In principle, such mixing, induced by CI, might

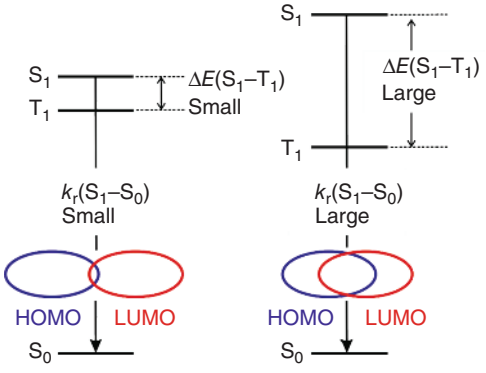

Figure 1.13 Schematic illustration of the relation between energy splitting $\Delta E(S_1–T_1)$ and the radiative decay rate $k_r(S_1–S_0)$ on the spatial overlap of HOMO and LUMO. *Source*: Ref. [31]. Reproduced with permission of Elsevier.

2 It is noted that the modified overlap $\int |\varphi_H||\varphi_L| \mathrm{d}V$ is a quantitative measure for the spatial overlap [170].

significantly increase the radiative rate of the lowest singlet–singlet transition without strongly altering the energy splitting $\Delta E(S_1-T_1)$. Presumably, such Cu(I) complexes may be developed in the future. In Section 1.6, we will address this challenge shortly again.

1.6 Design Strategies for Highly Efficient Ag(I)-Based TADF Compounds

In contrast to Cu(I) complexes, TADF materials based on Ag(I) are rarely reported [104, 106–109, 171]. This is related to the higher oxidation potential of Ag^+ compared with Cu^+ [172]. Accordingly, the 4d orbitals of Ag(I) complexes lie mostly energetically below ligand-centered (LC) orbitals. As a consequence, low-lying states of ^{3}LC character determine the emission properties [106, 173–176]. Thus, Ag(I) complexes often do not exhibit TADF, but long-lived phosphorescence and sometimes even slow ISC [175]. Therefore, designing Ag(I) complexes that show TADF represents an optimization task. In this respect, it is required to destabilize the energetically lower-lying 4d orbitals by an organic ligand with good electron-donating ability. This may be attainable with electron-donating bidentate phosphine ligands. Indeed, it has already been demonstrated that this strategy is successful. For example, $Ag_2Cl_2(dppb)_2$ **20** represents a blue light-emitting material that shows efficient TADF with $\Phi_{PL} = 97\%$, though with a relatively long decay time of $\tau(\text{TADF, 300 K}) = 15$ µs (Table 1.1) [107]. Another attractive ligand is *nido*-carborane-bis-(diphenylphosphine) (P_2-nCB) [177]. It coordinates via phosphine groups and, thus, induces substantial electron-donating character. Additionally, electron donation is strongly enhanced by the negative charge of the *nido*-carborane moiety. Suitable complexes can be built using the (P_2-nCB) ligand in combination with 1,10-phenanthroline (phen) or substituted phen ligands. Accordingly, a series of neutral Ag(I) complexes, referring to the numbers from **9** to **13**, is obtained (Table 1.1) [108, 109]. In this section, we want to focus on these Ag(phen)(P_2-nCB)-type compounds and to demonstrate key steps for designing a material that shows TADF behavior. Interestingly, by this strategy an efficiency breakthrough is reached [108, 109].

1.6.1 Ag(phen)(P_2-nCB): A First Step to Achieve TADF

DFT and TD-DFT calculations give an insight into electronic properties of Ag(phen)(P_2-nCB) **9**. The chemical structure as well as HOMO and LUMO plots are displayed in Figure 1.14. The calculations were performed for the optimized triplet T_1 state geometry. From the TD-DFT approach, it is indicated that the states S_1 and T_1 are dominated by HOMO → LUMO electronic transitions by 96% and 94%, respectively. Analysis of the frontier orbitals shows that the HOMO is mainly localized on the phosphines and the silver ion, whereas the LUMO is localized on the phen ligand. Accordingly, both states may be assigned to be of (metal + ligand L) to ligand L′ charge-transfer (^{1,3}MLL′CT) character. The small overlap of HOMO and LUMO suggests the occurrence

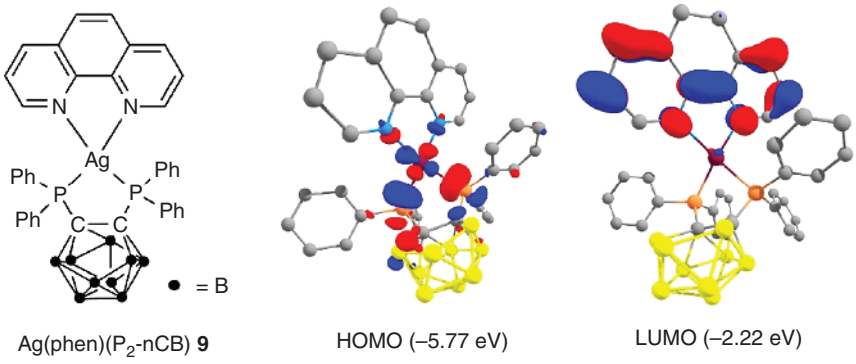

Figure 1.14 Chemical structure formula and calculated (M062X/def-2SVP) frontier orbital isosurface contour plots (iso-value = 0.05) for Ag(phen)(P_2-nCB) **9**. The calculations were carried out for the gas phase optimized (M06/def-2SVP) T_1 state geometry. *Source*: Ref. [109]. Reproduced with permission of Elsevier.

of a small exchange interaction between the unpaired electrons and, thus, a small $\Delta E(S_1-T_1)$ splitting. From TD-DFT calculations the energy gap of $\Delta E(S_1-T_1) = 1070\,cm^{-1}$ (133 meV) can be estimated from the energy difference between vertical electron transitions $S_0 \rightarrow S_1$ and $S_0 \rightarrow T_1$. This agrees approximately with the value of $725\,cm^{-1}$ (90 meV) roughly estimated from the shift of the emission peak maxima upon cooling (see below). Hence, this Ag(I) complex represents an interesting TADF candidate.

Figure 1.15 displays emission and absorption spectra of Ag(phen)(P_2-nCB) **9**. The absorption peak of low molar extinction ($3020\,M^{-1}\,cm^{-1}$) near 400 nm is

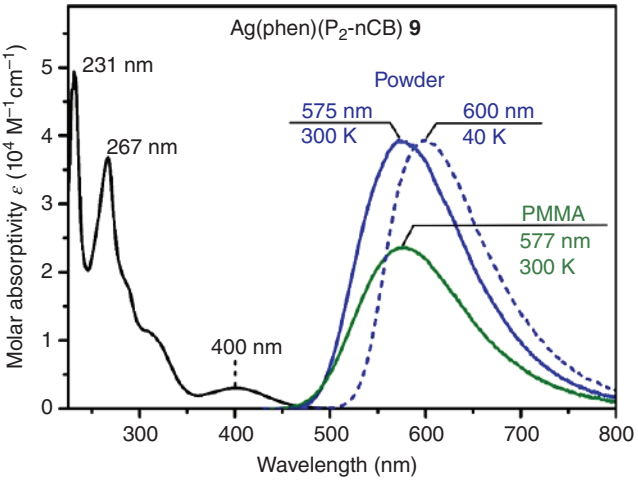

Figure 1.15 Emission and absorption spectra of Ag(phen)(P_2-nCB) **9** at different temperatures. The absorption spectrum is measured with a dichloromethane (DCM) solution of $\approx 10^{-5}$ M concentration at 300 K (black line). The emission spectra are shown in colored lines ($\lambda_{exc} = 410$ nm). The PMMA film was doped with ≈1 wt% of compound **9**. *Source*: Ref. [109]. Reproduced with permission of Elsevier.

assigned to the $S_0 \rightarrow S_1$ (^{1}MLL′CT) transition, while the structures of higher allowedness and higher energy are ascribed to LC transitions. (Compare also the TD-DFT results shown in the SI of Ref. [109].) The emission spectral bands are broad and unstructured as usually found for CT transitions. With temperature reduction from $T = 300$ to 40 K, a red shift of the peak maximum of the powder material from 575 to 600 nm (25 nm corresponding to 725 cm^{-1} or 90 meV) is observed. Such a behavior agrees well with the occurrence of TADF at 300 K. At ambient temperature, the emission stems dominantly from the singlet state S_1, while at $T = 40$ K, the TADF process is frozen out and only the lower-energy phosphorescence from the T_1 state occurs.

For completeness, it is noted that the slight red shift of the ambient temperature emission of the PMMA-doped emitter **9**, as compared with the powder material, is related to the lower rigidity of the PMMA film given by the emitter's environment. A corresponding behavior has already been discussed for Cu-based TADF compounds in Sections 1.3 and 1.4 as well as in the literature [31, 95].

1.6.2 Emission Quenching in Ag(phen)(P_2-nCB)

It is of particular importance for application of emitters in OLEDs that the photoluminescence quantum yield of the emitter should be as high as possible. However, for Ag(phen)(P_2-nCB), the values amount only to Φ_{PL}(powder, 300 K) = 36% and Φ_{PL}(PMMA doped, 300 K) = 26%, respectively (Table 1.6).[3] Therefore, it is of interest to understand why emission quenching is distinctly effective for this compound.

For Cu(I) complexes, it is well known that flattening distortions occur upon excitation of MLCT states (Section 1.3 and see Refs [31, 114, 117, 118, 121, 122, 178]). A similar behavior is also expected to be relevant for Ag(I) complexes. DFT geometry optimizations (M06/def2-SVP) show that the molecule in the lowest excited (relaxed) triplet state T_1 of Ag(phen)(P_2-nCB) **9** is distinctly twisted toward planarization as compared with the ground state geometry. This distortion cannot be characterized by one simple parameter, but in a rough description, one may take the change of the angle $\Delta\varphi$ between two planes placed into the molecular core of the complex (Figure 1.16). Related to such a distortion, the potential energy surfaces of the involved energy states are shifted significantly with respect to each other. This leads to an increase of the Franck–Condon factors between higher-lying vibrational states of the electronic ground state S_0 and the lower-lying vibrational states of the excited state. The larger the Franck–Condon factors, the more efficient are non-radiative relaxation processes [124–126]. Indeed, the emission quantum yield of compound **9** with a large value of $\Delta\varphi \approx 35°$ amounts only to $\Phi_{PL} = 36\%$, although the compound sits in a rigid crystalline (powder) environment.

These considerations lead to the suggestion to rigidify the emitter's structure by introducing intramolecular steric hindrances. Such an approach has already been successfully applied [9, 30, 31, 35, 92, 108, 109, 114, 119, 127]. (Compare

3 The emission quantum yield of Ag(phen)(P2-nCB) in degassed DCM solution is $\Phi_{PL} \ll 1\%$.

Table 1.6 Photophysical data that govern TADF properties of a series of Ag(I) complexes.

	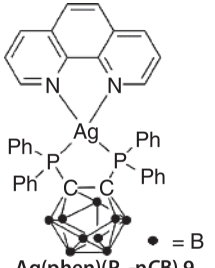 Ag(phen)(P_2-nCB) 9	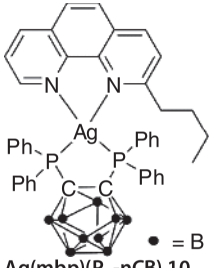 Ag(mbp)(P_2-nCB) 10	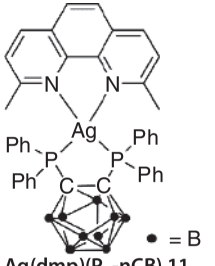 Ag(dmp)(P_2-nCB) 11	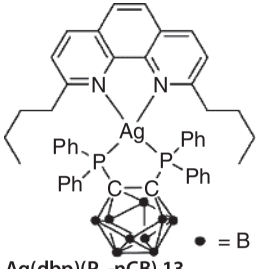 Ag(dbp)(P_2-nCB) 13
Φ_{PL}(300 K)	36%	70%	78%	100%
$f(S_1 \rightarrow S_0)$[a)]	0.0258	0.0478	0.0423	0.0536
$k_r(S_1 \rightarrow S_0)$[b)]	—	2.2×10^7 s^{-1}	2.2×10^7 s^{-1}	5.6×10^7 s^{-1}
τ^r(TADF, 300 K)[c)]	5.3 µs	2.9 µs	3.2 µs	1.4 µs
$\Delta E(S_1–T_1)$[d)]	—	640 cm^{-1}	650 cm^{-1}	650 cm^{-1}
λ_{max} (300 K)	575 nm	535 nm	537 nm	526 nm

a) TD-DFT calculated (M062X/def2-SVP) oscillator strength based on gas phase optimized (M06/def2-SVP) T_1 state geometries.
b) Radiative decay rate of the prompt fluorescence determined from the fit of Eq. (1.1) to experimental decay times at various temperatures.
c) Radiative decay time measured at 300 K, essentially representing TADF.
d) Energy gap between the lowest excited singlet and triplet states as determined from the fit of Eq. (1.1) to experimental decay times over a temperature range of $30 \leq T \leq 300$ K.

Source: Refs [108, 109]. Reproduced with permission of American Chemical Society.

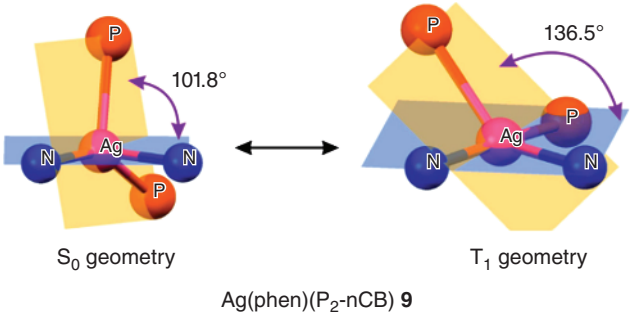

Figure 1.16 Schematic visualization of the geometry change between the electronic ground state S_0 and the triplet state T_1. Only the coordination core around the Ag ion is shown. The angles refer to the inclination between the P–Ag–P (orange) and the N–Ag–N (blue) planes. The charge transfer excitation induces a flattening distortion characterized by a model parameter of $\Delta\varphi \approx 35°$. The calculations were carried out on the M06/def2-SVP level of theory for the gas phase conditions. *Source*: Ref. [109]. Reproduced with permission of Elsevier.

also Section 1.3.) We will discuss this procedure in the next section, applying it to Ag(R-phen)(P_2-nCB), with R representing a substitution.

1.6.3 Sterical Hindrance. Tuning of the Emission Quantum Yield up to 100%

Several Ag(I) complexes comprising the P_2-nCB ligand in combination with a phenanthroline ligand, in each case differently substituted at the positions 2 and 9, are displayed in Table 1.6. The photophysical investigations show that with more bulky substituents on the phenanthroline ligand, the nonradiative decay rate decreases, and, hence, the photoluminescence quantum yield increases. For example, an increase from $\Phi_{PL} = 36\%$ found for Ag(phen)(P_2-nCB) **9** with an unsubstituted phen ligand to $\Phi_{PL} = 100\%$ for Ag(dbp)(P_2-nCB) **13** with the 2,9-di-*n*-butyl phenanthroline ligand is observed [108, 109]. The calculated model parameter $\Delta\varphi$, describing coarsely the flattening angle, correlates with this photophysical behavior, as was expected. Without sterical hindrance, the $\Delta\varphi$ parameter amounts to ≈35°, while for the compounds with sterical hindrance, the angle change is about three times smaller. For Ag(dbp)(P_2-nCB) **13**, for example, the $\Delta\varphi$ parameter amounts only to ≈12°. (Compare Figures 1.16 and 1.17.) According to the significantly lower geometry change upon CT excitation, the emission quantum yield increases drastically (Table 1.6).

The TD-DFT calculations (M062X/def2-SVP) carried out for the optimized T_1 state geometry reveal another important variation in the series of complexes shown in Table 1.6. The oscillator strength $f(S_0 \rightarrow S_1)$ of the $S_1 \rightarrow S_0$ electronic transition increases from $f = 0.0258$ for Ag(phen)(P_2-nCB) **9** to $f = 0.0536$ for Ag(dbp)(P_2-nCB) **13**, i.e. by a factor of more than two [109]. At the first sight, the reason for this increase is not obvious. However, in a computational model, as presented in Ref. [109], it can be shown that TD-DFT calculations carried out for Ag(phen)(P_2-nCB) **9**, fixed to the T_1 state geometry of Ag(dbp)(P_2-nCB)

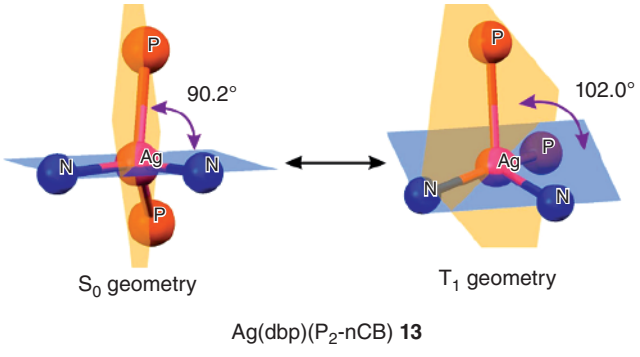

Figure 1.17 Schematic visualization of the geometry change between the electronic ground state S_0 and the triplet state T_1. Only the coordination core around Ag is shown. The angles refer to the inclination between the P–Ag–P (orange) and the N–Ag–N (blue) planes. The charge-transfer excitation induces a flattening distortion characterized by a model parameter $\Delta\varphi \approx 12°$. The geometry optimizations were carried out for gas phase conditions at the M06/def2-SVP level of theory. (Compare Figure 1.16.) *Source*: Ref. [109]. Adapted with permission of Elsevier.

13, gives the $S_0 \rightarrow S_1$ oscillator strength of $f = 0.0687$. This value is even higher than the value, calculated for compound Ag(dbp)(P_2-nCB) **13** itself. Obviously, the effect of the complex geometry on the $S_1 \rightarrow S_0$ oscillator strength is superior to the electronic influence of the substituents on positions 2 and 9 of the 1,10-phenanthroline ligand [109].

The increase of the calculated oscillator strength of the series of Ag(I) complexes should also be displayed in the experimentally determined radiative rate (that is, proportional to the oscillator strength). Indeed, the radiative rates $k_r(S_1 \rightarrow S_0)$ (Table 1.6) show a similar increase as is seen, for example, when Ag(mbp)(P_2-nCB) with $k_r(S_1–S_0) = 2.2 \times 10^7$ s^{-1} is compared with Ag(dbp)(P_2-nCB) with $k_r(S_1–S_0) = 5.6 \times 10^7$ s^{-1}.

In summary, the drastic increase of the emission quantum yield in the series of Ag(I) complexes arranged in Table 1.6 is induced by two different effects: (i) Increasing sterical hindrance strongly reduces nonradiative relaxation. (ii) In parallel, the 2,9-substitutions stabilize a complex geometry that leads to a high radiative rate. Both effects are responsible in a very favorite way for attaining the high emission quantum yield of $\Phi_{PL} = 100\%$ for Ag(dpb)(P_2-nCB).

For completeness, we also calculated the $S_0 \rightarrow S_1$ oscillator strengths for Cu(I) complexes with the same ligands. For example, TD-DFT calculation (M062X/def2-SVP) carried out for compound Cu(dbp)(P_2-nCB) in gas phase for the T_1 state geometry (M06/def2-SVP) gives an oscillator strength value of $f = 0.0660$, while the value for the corresponding Ag(dbp)(P_2-nCB) complex amounts to $f = 0.0536$. Obviously, the change of allowedness affected by replacement of Ag(I) through Cu(I) is not very distinct.[4]

Guided by this result, it seems to be justified to relate properties based on oscillator strengths of the $S_1 \leftrightarrow S_0$ transitions of Ag(I) complexes to trends that

4 The emission quantum yield of Cu(dbp)(P_2-nCB) powder is relatively low ($\Phi_{PL} = 16\%$). Therefore, this material is not suitable for OLED applications.

are observed for Cu(I) complexes. In particular, comparison to the relation between the energy splitting $\Delta E(S_1–T_1)$ and the radiative rate $k_r(S_1–S_0)$, as displayed in Figure 1.12 (Section 1.5) for Cu(I) complexes, elucidates an interesting result. Inserting the data found for Ag(dbp)(P_2-nCB) with $\Delta E(S_1–T_1) = 650\,cm^{-1}$ and $k_r(S_1–S_0) = 5.6 \times 10^7\ s^{-1}$ (Table 1.6), it becomes obvious that these data do not fit. The rate of the Ag(I) complex is about one order of magnitude higher than expected from the relation shown in Figure 1.12. This result is highly interesting, since it indicates how to develop new materials that break the restrictions imposed by the simple quantum mechanical model presented in Section 1.5. Apparently, the singlet state S_1 wave function of the discussed Ag(I) complexes are not simply given by the HOMO–LUMO excitation, but are distinctly modified by configurational interaction. This means that higher-lying singlet states, resulting from other configurations, mix and thus induce significantly larger $S_1 \rightarrow S_0$ transition rates. Further quantum mechanical investigations have to be carried out in this respect. Nevertheless, these results represent a guideline for the development of materials with shorter TADF decay time, as it has already been demonstrated for Ag(dbp)(P_2-nCB) **13** [108].

1.6.4 Detailed Characterization of Ag(dbp)(P_2-nCB)

The TADF properties of Ag(dbp)(P_2-nCB) **13** are highly attractive due to its photoluminescence quantum yield of $\Phi_{PL} = 100\%$ and the very short decay time of $\tau(TADF) = 1.4\ \mu s$. Therefore, in this section, we will focus on a detailed characterization of the compound's emission properties.

The lowest excited singlet S_1 and triplet T_1 states predominantly originate from the HOMO → LUMO transition (92%), slightly less than found for Ag(phen)(P_2-nCB) **9**. The HOMO is mainly composed of silver (13%) and phosphorus (47%) orbitals, while the LUMO represents a π^* orbital of the dbp ligand (Figure 1.18). Thus, we can assign the two lowest excited states as ^{1,3}(MLL′CT) states with L and L′ representing P_2-nCB and dbp, respectively. According to the TD-DFT calculations carried out for the optimized T_1 state geometry of Ag(dbp)(P_2-nCB) **13**, the energy separation $\Delta E(S_1–T_1)$ can be estimated to 0.15 eV (≈1200 cm^{-1}). This represents an upper bound that is obtained from vertical excitations of $S_0 \rightarrow S_1$ and $S_0 \rightarrow T_1$ transitions, respectively. The calculated value is largely in agreement with the experimentally determined activation energy of $\Delta E(S_1–T_1) = 650\,cm^{-1}$ (see below).

The *n*-butyl substitutions at the 2,9-positions of the phen ligand lead to a distinct sterical hindrance with respect to a geometry change upon the CT excitation. DFT computations show that this flattening distortion is much less expressed than found for Ag(phen)(P_2-nCB). (Compare Figures 1.16 and 1.17.) As a consequence, it is expected that the emission quantum yield of the more rigid complex Ag(dbp)(P_2-nCB) **13** is higher than that of Ag(phen)(P_2-nCB), as already discussed above and as experimentally found.[5]

---

5 The molecular rigidity of Ag(dbp)(P_2-nCB) is largely maintained, even if the complex is doped in PMMA, in contrast to most other TADF compounds (compare Section 1.3 and Ref. [95]) For Ag(dbp)(P_2-nCB) doped in PMMA, Φ_{PL} drops from 100% (powder) only to 85% (Table 1.7).

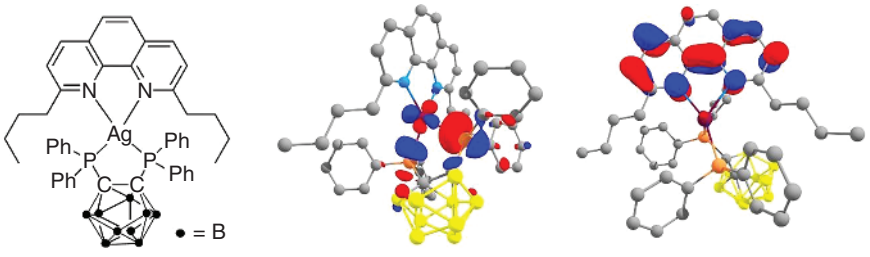

Ag(dbp)(P_2-nCB) **13**

Figure 1.18 Chemical structure formula and calculated (M062X/def2-SVP) isosurface contour plots (iso-value = 0.05) of the frontier orbitals of Ag(dbp)(P_2-nCB) **13**. The calculations were carried out for the gas phase optimized (M06/def2-SVP) T_1 state geometry. *Source*: Ref. [108]. Reproduced with permission of American Chemical Society.

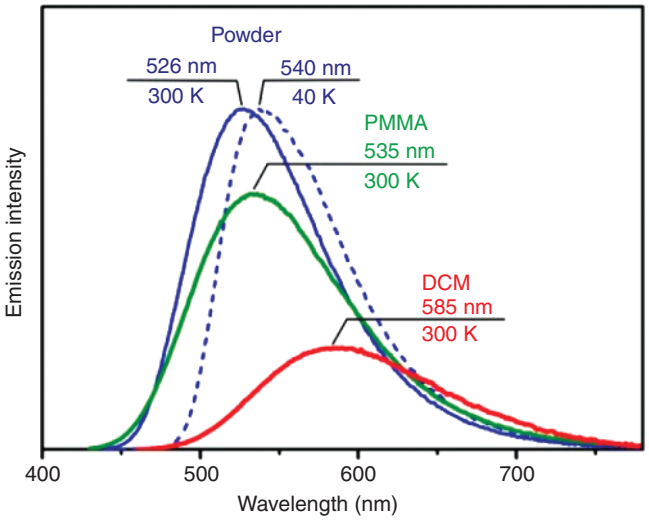

Figure 1.19 Emission spectra of Ag(dbp)(P_2-nCB) **13**. The measurements were carried out under different conditions, as marked in the diagram. Concentrations: PMMA: $c \approx 1$ wt%, dissolved in dichloromethane (DCM): $c \approx 10^{-5}$ M. $\lambda_{exc} = 410$ nm. *Source*: Ref. [108]. Reproduced with permission of American Chemical Society.

Figure 1.19 displays the emission spectra of Ag(dbp)(P_2-nCB) **13**. The spectra are broad and unstructured as expected for CT transitions. Even cooling to $T = 1.5$ K does not lead to any better resolution (not shown). However, application of methods based on the temperature dependence of the emission decay time reveals additional information, as will be demonstrated below. For the powder material, a blue shift is observed with temperature increase from $T = 40$ K (T_1 emission) to $T = 300$ K (S_1 emission) of $\Delta\lambda = 14$ nm corresponding to 490 cm^{-1} (60 meV). This value fits approximately to the activation energy of $\Delta E(S_1 - T_1) = 650\ cm^{-1}$ (80 meV) as determined below. However, it is noted that the emission spectra represent transitions between Franck–Condon states, and

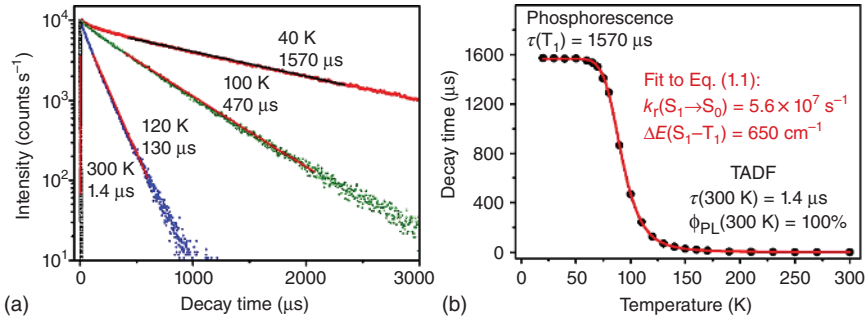

Figure 1.20 (a) Luminescence decay curves of Ag(dbp)(P_2-nCB) **13** powder measured at different temperatures. (b) Luminescence decay time (τ) plotted versus temperature. The values of $k(S_1 \rightarrow S_0) = 5.6 \times 10^7$ s^{-1} (18 ns) and $\Delta E(S_1–T_1) = 650$ cm^{-1} result from a fit of Eq. (1.1) to the experimental $\tau(T)$ data, with $\tau(T_1)$ fixed to 1570 µs as determined directly for $T < 60$ K (plateau). $\lambda_{exc} = 378$ nm, diode laser PB-375 L, and pulse width = 100 ps. *Source*: Adapted with permission from Ref. [108]. Copyright © 2017, American Chemical Society.

therefore the shift of emission spectra is not very reliable to assess the $\Delta E(S_1–T_1)$ gap, especially when the excited states are of CT character.

Detailed information on the electronic structure and the relevant decay processes can be obtained from time-resolving measurements, as already shown in previous sections. Figure 1.20a shows almost monoexponential emission decay curves measured at different temperatures. In Figure 1.20b, the decay times are plotted versus temperature. In the temperature range of $20\,K \leq T \leq 60\,K$, a constant value of 1570 µs is observed (plateau). With this value and the low-temperature emission quantum yield of $\Phi_{PL}(77\,K) = 87\%$ (Table 1.7), one can determine the radiative rate to $k_r(40\,K) = 5.5 \times 10^2$ s^{-1} (applying Eq. (1.3), whereby it is assumed that the quantum yield at $T = 40$ K is the same as the measured one at $T = 77$ K). With temperature increase to $T = 300$ K, the decay time decreases drastically to $\tau(300\,K) = 1.4$ µs (at $\Phi_{PL} = 100\%$). Accordingly, the radiative rate increases by a factor of about 1300 to $k_r(300\,K) = 7.1 \times 10^5$ s^{-1}. Obviously, such a change has to be related to the involvement of different electronic transitions at low and high temperature, respectively. At low temperature, the emission is a phosphorescence from the T_1 state, and at ambient temperature it represents TADF from the S_1 state.

The monoexponentiality of the decay curves indicates fast thermalization between the involved energy states due to fast up- and down-ISC and small inhomogeneities (small variations of $\Delta E(S_1–T_1)$) of the compounds in the powder material. In this situation, the emission decay time $\tau(T)$ of a molecular system of two excited energy states, T_1 and S_1, can be expressed by Eq. (1.1). The fit of this equation to the experimental data (Figure 1.20b) gives the activation energy of $\Delta E(S_1–T_1) = 650$ cm^{-1} (80 meV) and the radiative rate of the prompt fluorescence of $k_r(S_1 \rightarrow S_0) = 5.6 \times 10^7$ s^{-1}. Formally, this value corresponds to a fluorescence decay time of $\tau(S_1) = 18$ ns. However, the related prompt fluorescence is not directly observed, since the processes of ISC from S_1 to T_1 are about three orders of magnitude faster (compare Ref. [118, 121, 133]) [134].

Table 1.7 Emission data for Ag(I) complexes as powder materials and doped in PMMA measured at different temperatures.

	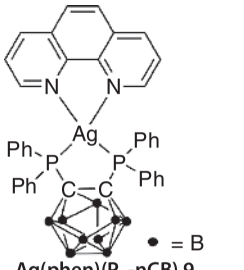 Ag(phen)(P_2-nCB) 9		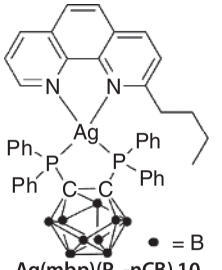 Ag(mbp)(P_2-nCB) 10		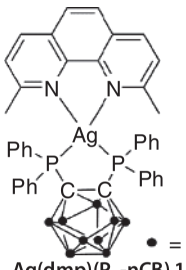 Ag(dmp)(P_2-nCB) 11		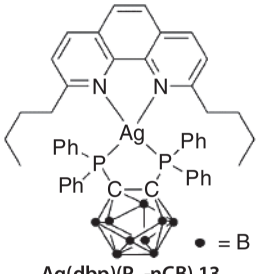 Ag(dbp)(P_2-nCB) 13	
	Powder	**PMMA**	**Powder**	**PMMA**	**Powder**	**PMMA**	**Powder**	**PMMA**
λ_{max}(300 K)	575 nm	577 nm	535 nm	555 nm	537 nm	540 nm	526 nm	535 nm
Φ_{PL}(300 K)	36%	26%	70%	58%	78%	75%	100%	85%
τ(300 K)	2.0 µs		2.0 µs		2.8 µs		1.4 µs	
k_r(300 K)	1.8×10^5 s^{-1}		3.5×10^5 s^{-1}		2.8×10^5 s^{-1}		7.1×10^5 s^{-1}	
k_{nr} (300 K)	3.2×10^5 s^{-1}		1.5×10^5 s^{-1}		0.79×10^5 s^{-1}		$<0.21\times10^5$ s^{-1} [b]	
Φ_{PL}(77 K)	15%		70%		68%		87%	
τ(77 K)	270 µs		1390 µs		804 µs		1300 µs	
k_r(77 K)	5.6×10^2 s^{-1}		5×10^2 s^{-1}		8.5×10^2 s^{-1}		6.7×10^2 s^{-1}	
k_{nr}(77 K)	3.1×10^3 s^{-1}		2.2×10^2 s^{-1}		3.9×10^2 s^{-1}		1×10^2 s^{-1}	
τ(T_1, 40 K)			1600 µs		885 µs		1570 µs	
k_r($S_1 \rightarrow S_0$)[a]			2.2×10^7 s^{-1}		2.8×10^7 s^{-1}		5.6×10^7 s^{-1}	
ΔE(S_1–T_1)[a]			640 cm^{-1}		650 cm^{-1}		650 cm^{-1}	

a) Determined from the fit of experimental luminescence decay times according to Eq. (1.1), measured for a powder sample at different temperatures.
b) Determined assuming 3% error for the measured Φ_{PL} value, which would allow $\Phi_{PL} = 97\%$.

The experimental value of $k(S_1–S_0) = 5.6 \times 10^7$ s^{-1} found for the prompt fluorescence rate is remarkably large. Cu(I) complexes investigated so far (and that have comparable $\Delta E(S_1–T_1)$ splittings) exhibit only rates that are one order of magnitude smaller [31]. (See Section 1.5, Figure 1.12.) Thus, the high (prompt) fluorescence rate can be identified as a key feature that leads to the exceptionally fast TADF decay time of Ag(dbp)(P_2-nCB). This behavior fits perfectly to the large oscillator strength that is calculated for the $S_1 \rightarrow S_0$ transition. (Compare the discussion presented above in this section.)

Photophysical data for Ag(dbp)(P_2-nCB) **13** are summarized in Table 1.7 and in an energy level diagram shown in Figure 1.21. Herein, the material's properties are highlighted: At low temperature ($T < 60$ K), one observes only long-living phosphorescence as the $T_1 \rightarrow S_0$ transition decays with $\tau = 1570$ µs. Such a long phosphorescence decay time is not unusual for Ag(I) or Cu(I) compounds [31, 33, 96, 107, 179]. It displays the spin forbiddenness of this transition. The reason is that SOC to singlet states is weak. According to the discussion presented in Refs [108, 109], the next higher-lying singlet state (S_4) that exhibits a different 4d orbital character than the T_1 state and that can induce SOC (following general quantum mechanical rules) [70–77] is energetically far ($\Delta E(S_4–T_1) = 1.57$ eV). Therefore, the singlet character mixed into the T_1 state is very small. As already mentioned in Section 1.4, SOC via the S_1 state can be neglected.

With temperature increase, the S_1 state is populated according to the thermal energy $k_B T$. As a consequence, the decay time decreases and a spectral blue shift is observed. This represents the TADF effect. The corresponding activation energy, as determined from the decay time plot (Figure 1.20b), amounts to $\Delta E(S_1–T_1) = 650$ cm^{-1}. This energy separation is not very small (compare compound **2**, Section 1.4), but the $S_1 \rightarrow S_0$ transition rate is much higher than for any other organometallic TADF material (with comparable $\Delta E(S_1–T_1)$ values). Thus, the TADF decay time drops to the record value of τ(TADF, 300 K) = 1.4 µs. Moreover, the Ag(I) complex represents the first TADF material with a radiative decay time comparable to those of Ir(III) complexes [1, 69, 70, 86, 89] that have become famous for OLED applications.

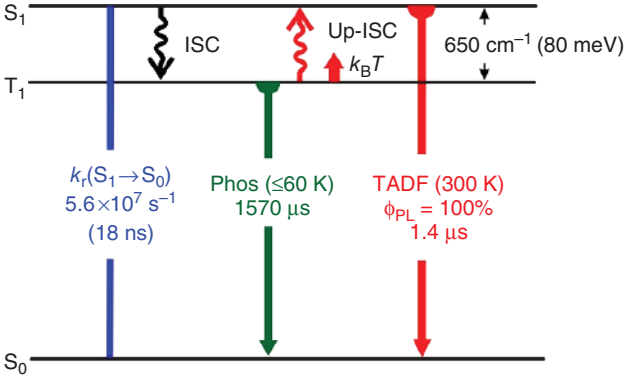

Figure 1.21 Energy level diagram and decay times/rates for Ag(dbp)(P_2-nCB) **13** powder. Frequently, up-ISC is also denoted as reverse ISC (rISC). *Source*: Ref. [108]. Adapted with permission of American Chemical Society.

This short TADF decay time or the related very large radiative decay rate of $k_r(\text{TADF, } 300\,\text{K}) = 7.1 \times 10^5\ \text{s}^{-1}$ is responsible for the high quantum yield of $\Phi_{PL} = 100\%$, measured at $T = 300\,\text{K}$. For completeness, it is mentioned that the quantum yield at $T = 77\,\text{K}$ amounts to only $\Phi_{PL}(77\,\text{K}) = 87\%$, since at that temperature the decay time is with $\tau(77\,\text{K}) = 1300\,\mu\text{s}$ relatively long, leading to a radiative rate of only $k_r(77\,\text{K}) = 6.7 \times 10^2\ \text{s}^{-1}$. Using Eq. (1.2), the nonradiative rate for this temperature is determined to $k_{nr} = 1 \times 10^2\ \text{s}^{-1}$. Thus at 77 K, the non-radiative process can moderately compete with the radiative process. But at ambient temperature, the TADF rate predominates by about three orders of magnitude. Hence, nonradiative processes are no longer relevant.

1.7 Conclusion and Future Perspectives

In this chapter, we study TADF material design based on photophysical properties investigated for a large number of compounds, in particular, with respect to OLED applications. Especially, we focus on photoluminescence properties and on the crucial requirement of designing materials that exhibit short emission decay times (high radiative rates), obviously at high emission quantum yields. The decay time should be as short as possible in order to minimize nonradiative quenching, saturation effects, and, in particular, chemical reactions that might occur in the excited state. Thus, short TADF decay time will help to increase the OLED device lifetime. Here, we discuss important molecular or photophysical parameters and analyze their impact on the TADF decay time. For example, it is well known that the energy separation $\Delta E(S_1{-}T_1)$ between the lowest excited singlet state S_1 and triplet state T_1 should be as small as possible. Accordingly, we present detailed photophysical properties of two case studies referring to materials that exhibit a large $\Delta E(S_1{-}T_1)$ value of $1000\,\text{cm}^{-1}$ (120 meV) and a small one of $370\,\text{cm}^{-1}$ (46 meV), respectively. From these studies – extended by investigations of photophysical properties of many other Cu(I) TADF compounds – we can show, however, that small $\Delta E(S_1{-}T_1)$ is not a sufficient requirement for short TADF decay time. High allowedness of the transition between the emitting S_1 state and the electronic ground state S_0, expressed by the radiative rate $k_r(S_1 \rightarrow S_0)$, is also very important. This has often been disregarded. However, mostly small $\Delta E(S_1{-}T_1)$ is related to a small $k_r(S_1 \rightarrow S_0)$. As a consequence, a reduction of τ(TADF) to below a few microsecond might be problematic. This relation results from an investigation of a large number of Cu(I) complexes and basic quantum mechanical considerations. However, these studies are based on a situation, in fact a very frequent one, in which the involved states, S_1 and T_1, stem from the same HOMO–LUMO excitation. Other higher-lying singlet states from which the $S_1 \rightarrow S_0$ transition might borrow allowedness are energetically too far from the S_1 state. However, new materials can be designed for which this disadvantage is not prevailing. Very probably, the new TADF compound, Ag(dbp)(P_2-nCB), represents such an example. Indeed, we obtained a TADF record material with $\tau(\text{TADF}) = 1.4\,\mu\text{s}$ at 100% emission quantum yield, as discussed in Section 1.6.

As a consequence, it is an important issue for future developments of TADF materials with even shorter decay times to focus on the different effects of (i) reducing the overlap of HOMO and LUMO, which leads to a smaller exchange interaction (small $\Delta E(S_1-T_1)$) and (ii) to provide other energetically low-lying singlet states from which the $S_1 \rightarrow S_0$ transition can borrow oscillator strength. For completeness, it is remarked that a different strategy to reduce the emission decay time can also be successful. It has been shown that an increase of SOC with respect to the T_1 state, leading to an increase of the $T_1 \rightarrow S_0$ phosphorescence rate, will open another radiative decay path. In this situation, the phosphorescence decay path is added to the TADF path [144]. Accordingly, the overall emission decay time is also significantly reduced [31, 97].

For completeness, it is mentioned that similar design rules (with the exception of increasing the phosphorescence decay rate) are also valid for purely organic TADF materials. Thus, recently it was possible to develop compounds by minimizing even a residual donor-acceptor hyper-conjugation. These compounds show extremely small $\Delta E(S_1-T_1)$ values of $\leq 10\ cm^{-1}$ (≈ 1 meV) ($\ll k_B T$ at ambient temperature) and that carry sufficient $S_1 \rightarrow S_0$ allowedness to result in a decay time regime of only a few 100 ns. Interestingly, at this small energy separation, thermal activation is not a key property. All excitons that populate the triplet state (75%) are transferred directly by ISC to the singlet state S_1 (that is populated independently by 25%). This new mechanism of *Direct Singlet Harvesting* will lead us to beyond TADF and might be successful for next generation OLED applications [180–183]. An equivalent design strategy as developed for the organic materials could also be successful for organometallic TADF materials in future.

Acknowledgments

The authors thank the German Ministry of Education and Research for financial support in the scope of the cyCESH project (FKN 13N12668). R.C. thanks the European Research Council (ERC) for support in the framework of the MSCA RISE Project no. 645628. M.Z.S. thanks Professor Duncan Bruce (York) and the University of York for their help with computational facilities. Moreover, we thank our cooperation partners for fruitful collaborations. This includes the research groups of Prof. Dr. Chensheng Ma (Shenzhen University, China), Prof. Dr. Wai-Ming Kwok (Hong Kong Polytechnic University, Hong Kong), and Prof. Dr. Thomas A. Niehaus (Claude Bernard University, Lyon, France). In addition, we acknowledge the German Academic Exchange Service (DAAD) and the Bavaria California Technology Center (BaCaTec) for giving us the opportunity to establish and maintain our collaborations.

References

1 Yersin, H. (2008). *Highly Efficient OLEDs with Phosphorescent Materials*. Weinheim: Wiley-VCH.
2 Brütting, W. and Adachi, C. (2012). *Physics of Organic Semiconductors*. Weinheim: Wiley-VCH.

3 Kim, Y., Park, S., Lee, Y.H., Jung, J., Yoo, S., and Lee, M.H. (2016). Homoleptic Tris-cyclometalated iridium complexes with substituted o-carboranes: green phosphorescent emitters for highly efficient solution-processed organic light-emitting diodes. *Inorg. Chem.* 55: 909–917.
4 Liu, Z., Qiu, J., Wei, F., Wang, J., Liu, X., Helander, M.G., Rodney, S., Wang, Z., Bian, Z., Lu, Z., Thompson, M.E., and Huang, C. (2014). Simple and high efficiency phosphorescence organic light-emitting diodes with codeposited copper(I) emitter. *Chem. Mater.* 26: 2368–2373.
5 Zhang, X.Q., Xie, Y.M., Zheng, Y., Liang, F., Wang, B., Fan, J., and Liao, L.S. (2016). Highly phosphorescent platinum(II) complexes based on rigid unsymmetric tetradentate ligands. *Org. Electron. Phys. Mater. Appl.* 32: 120–125.
6 Kim, J., Lee, K.H., Lee, S.J., Lee, H.W., Kim, Y.K., Kim, Y.S., and Yoon, S.S. (2016). Red phosphorescent bis-cyclometalated iridium complexes with fluorine-, phenyl-, and fluorophenyl-substituted 2-arylquinoline ligands. *Chem. Eur. J.* 22: 4036–4045.
7 Wong, M.Y., Hedley, G.J., Xie, G., Kölln, L.S., Samuel, I.D.W., Pertegás, A., Bolink, H.J., and Zysman-Colman, E. (2015). Light-emitting electrochemical cells and solution-processed organic light-emitting diodes using small molecule organic thermally activated delayed fluorescence emitters. *Chem. Mater.* 27: 6535–6542.
8 Minaev, B., Baryshnikov, G., and Agren, H. (2014). Principles of phosphorescent organic light emitting devices. *Phys. Chem. Chem. Phys.* 16: 1719–1758.
9 Yersin, H., Rausch, A.F., and Czerwieniec, R. (2012). Organometallic emitters for OLEDs. triplet harvesting, singlet harvesting, case structures, and trends. In: *Physics of Organic Semiconductors*, 2e (ed. W. Brütting and C. Adachi), 371–425. Weinheim: Wiley-VCH.
10 Sun, Y., Giebink, N.C., Kanno, H., Ma, B., Thompson, M.E., and Forrest, S.R. (2006). Management of singlet and triplet excitons for efficient white organic light-emitting devices. *Nature* 440: 908–912.
11 Adachi, C., Baldo, M.A., Thompson, M.E., and Forrest, S.R. (2001). Nearly 100% internal phosphorescence efficiency in an organic light emitting device. *J. Appl. Phys.* 90: 5048–5051.
12 Lamansky, S., Djurovich, P., Murphy, D., Abdel-Razzaq, F., Lee, H.E., Adachi, C., Burrows, P.E., Forrest, S.R., and Thompson, M.E. (2001). Highly phosphorescent bis-cyclometalated iridium complexes: synthesis, photophysical characterization, and use in organic light emitting diodes. *J. Am. Chem. Soc.* 123: 4304–4312.
13 Kim, S.Y., Jeong, W.I., Mayr, C., Park, Y.S., Kim, K.H., Lee, J.H., Moon, C.K., Brütting, W., and Kim, J.J. (2013). Organic light-emitting diodes with 30% external quantum efficiency based on a horizontally oriented emitter. *Adv. Funct. Mater.* 23: 3896–3900.
14 Schmidt, T.D., Reichardt, L.J., Rausch, A.F., Wehrmeister, S., Scholz, B.J., Mayr, C., Wehlus, T., Ciarnáin, R.M., Danz, N., Reusch, T.C.G., and Brütting, W. (2014). Extracting the emitter orientation in organic

light-emitting diodes from external quantum efficiency measurements. *Appl. Phys. Lett.* 105: doi: 10.1063/1.4891680.

15 Cherpak, V., Stakhira, P., Minaev, B., Baryshnikov, G., Stromylo, E., Helzhynskyy, I., Chapran, M., Volyniuk, D., Tomkuté-Lukšiené, D., Malinauskas, T., Getautis, V., Tomkeviciene, A., Simokaitiene, J., and Grazulevicius, J.V. (2014). Efficient "warm-white" OLEDs based on the phosphorescent bis-cyclometalated iridium(III) complex. *J. Phys. Chem. C* 118: 11271–11278.

16 Tuong Ly, K., Chen-Cheng, R.-W., Lin, H.-W., Shiau, Y.-J., Liu, S.-H., Chou, P.-T., Tsao, C.-S., Huang, Y.-C., and Chi, Y. (2016). Near-infrared organic light-emitting diodes with very high external quantum efficiency and radiance. *Nat. Photonics* 11: 63–69.

17 Ma, D., Zhang, C., Qiu, Y., and Duan, L. (2017). Sustainable phosphorescence based on solution-processable and vacuum-sublimable cationic ruthenium(II) complexes achieved by counter-ion control. *Org. Electron.* 42: 194–202.

18 Zhang, J., Zhu, X., Zhong, A., Jia, W., Wu, F., Li, D., Tong, H., Wu, C., Tang, W., Zhang, P., Wang, L., and Han, D. (2017). New platinum(II) one-armed Schiff base complexes for blue and orange PHOLEDs applications. *Org. Electron.* 42: 153–162.

19 Salehi, A., Ho, S., Chen, Y., Peng, C., Yersin, H., and So, F. (2017). Highly efficient organic light-emitting diode using a low refractive index electron transport layer. *Adv. Opt. Mater.* 5: 1700197.

20 Yang, C.H., Beltran, J., Lemaur, V., Cornil, J., Hartmann, D., Sarfert, W., Fröhlich, R., Bizzarri, C., and De Cola, L. (2010). Iridium metal complexes containing N-heterocyclic carbene ligands for blue-light-emitting electrochemical cells. *Inorg. Chem.* 49: 9891–9901.

21 Henwood, A.F. and Zysman-Colman, E. (2016). Luminescent iridium complexes used in light-emitting electrochemical cells (LEECs). *Top. Curr. Chem.* 374: 36.

22 Pal, A.K., Cordes, D.B., Slawin, A.M.Z., Momblona, C., Ortí, E., Samuel, I.D.W., Bolink, H.J., and Zysman-Colman, E. (2016). Synthesis, properties, and light-emitting electrochemical cell (LEEC) device fabrication of cationic Ir(III) complexes bearing electron-withdrawing groups on the cyclometallating ligands. *Inorg. Chem.* 55: 10361–10376.

23 Ertl, C.D., Bolink, H.J., Housecroft, C.E., Constable, E.C., Ortí, E., Junquera-Hernández, J.M., Neuburger, M., Shavaleev, N.M., Nazeeruddin, M.K., and Vonlanthen, D. (2016). Bis-sulfone- and bis-sulfoxide-spirobifluorenes: polar acceptor hosts with tunable solubilities for blue-phosphorescent light-emitting devices. *Eur. J. Org. Chem.* 2016: 2037–2047.

24 Henwood, A.F. and Zysman-Colman, E. (2017). Lessons learned in tuning the optoelectronic properties of phosphorescent iridium(III) complexes. *Chem. Commun.* 53: 807–826.

25 Ertl, C.D., Momblona, C., Pertegás, A., Junquera-Hernández, J.M., La-Placa, M.G., Prescimone, A., Ortí, E., Housecroft, C.E., Constable, E.C., and Bolink, H.J. (2017). Highly stable red-light-emitting electrochemical cells. *J. Am. Chem. Soc.* 139: 3237–3248.

26 Martir, D.R., Momblona, C., Pertegás, A., Cordes, D.B., Slawin, A.M.Z., Bolink, H.J., and Zysman-Colman, E. (2016). Chiral iridium(III) complexes in light-emitting electrochemical cells: exploring the impact of stereochemistry on the photophysical properties and device performances. *ACS Appl. Mater. Interfaces* 8: 33907–33915.

27 Armaroli, N., Accorsi, G., Holler, M., Moudam, O., Nierengarten, J.F., Zhou, Z., Wegh, R.T., and Welter, R. (2006). Highly luminescent Cu^{I} complexes for light-emitting electrochemical cells. *Adv. Mater.* 18: 1313–1316.

28 Tang, S. and Edman, L. (2016). Light-emitting electrochemical cells: a review on recent progress. *Top. Curr. Chem.* 374: 40. doi: 10.1007/s41061-016-0040-4.

29 Che, C.M., Kwok, C.C., Lai, S.W., Rausch, A.F., Finkenzeller, W.J., Zhu, N., and Yersin, H. (2010). Photophysical properties and OLED applications of phosphorescent platinum(II) schiff base complexes. *Chem. Eur. J.* 16: 233–247.

30 Leitl, M.J., Zink, D.M., Schinabeck, A., Baumann, T., Volz, D., and Yersin, H. (2016). Copper(I) complexes for thermally activated delayed fluorescence: from photophysical to device properties. *Top. Curr. Chem.* 374: 25.

31 Czerwieniec, R., Leitl, M.J., Homeier, H.H.H., and Yersin, H. (2016). Cu(I) complexes – thermally activated delayed fluorescence. Photophysical approach and material design. *Coord. Chem. Rev.* 325: 2–28.

32 Hong, X., Wang, B., Liu, L., Zhong, X.X., Li, F.B., Wang, L., Wong, W.Y., Qin, H.M., and Lo, Y.H. (2016). Highly efficient blue–green neutral dinuclear copper(I) halide complexes containing bidentate phosphine ligands. *J. Lumin.* 180: 64–72.

33 Leitl, M.J., Küchle, F.-R., Mayer, H.A., Wesemann, L., and Yersin, H. (2013). Brightly blue and green emitting Cu(I) dimers for singlet harvesting in OLEDs. *J. Phys. Chem. A* 117: 11823–11836.

34 Leitl, M.J., Krylova, V.A., Djurovich, P.I., Thompson, M.E., and Yersin, H. (2014). Phosphorescence versus thermally activated delayed fluorescence. Controlling singlet-triplet splitting in brightly emitting and sublimable Cu(I) compounds. *J. Am. Chem. Soc.* 136: 16032–16038.

35 Linfoot, C.L., Leitl, M.J., Richardson, P., Rausch, A.F., Chepelin, O., White, F.J., Yersin, H., and Robertson, N. (2014). Thermally activated delayed fluorescence (TADF) and enhancing photoluminescence quantum yields of $[Cu^{I}(diimine)(diphosphine)]^{+}$ complexes – photophysical, structural, and computational studies. *Inorg. Chem.* 53: 10854–10861.

36 Zhang, Q., Zhou, Q., Cheng, Y., Wang, L., Ma, D., Jing, X., and Wang, F. (2004). Highly efficient green phosphorescent organic light-emitting diodes based on CuI complexes. *Adv. Mater.* 16: 432–436.

37 Zink, D.M., Volz, D., Baumann, T., Mydlak, M., Flügge, H., Friedrichs, J., Nieger, M., and Bräse, S. (2013). Heteroleptic, dinuclear copper(I) complexes for application in organic light-emitting diodes. *Chem. Mater.* 25: 4471–4486.

38 Volz, D., Zink, D.M., Bocksrocker, T., Friedrichs, J., Nieger, M., Baumann, T., Lemmer, U., and Bräse, S. (2013). Molecular construction kit for

tuning solubility, stability and luminescence properties: heteroleptic MePyrPHOS-copper iodide-complexes and their application in organic light-emitting diodes. *Chem. Mater.* 25: 3414–3426.

39 Volz, D., Baumann, T., Flügge, H., Mydlak, M., Grab, T., Bachle, M., Barner-Kowollik, C., and Bräse, S. (2012). Auto-catalysed crosslinking for next-generation OLED-design. *J. Mater. Chem.* 22: 20786–20790.

40 Wallesch, M., Volz, D., Zink, D.M., Schepers, U., Nieger, M., Baumann, T., and Bräse, S. (2014). Bright coppertunities: multinuclear Cu^{I} complexes with N–P ligands and their applications. *Chem. Eur. J.* 20: 6578–6590.

41 Volz, D., Chen, Y., Wallesch, M., Liu, R., Fléchon, C., Zink, D.M., Friedrichs, J., Flügge, H., Steininger, R., Göttlicher, J., Heske, C., Weinhardt, L., Bräse, S., So, F., and Baumann, T. (2015). Bridging the efficiency gap: fully bridged dinuclear Cu(I)-complexes for singlet harvesting in high-efficiency OLEDs. *Adv. Mater.* 27: 2538–2543.

42 Osawa, M., Hoshino, M., Hashimoto, M., Kawata, I., Igawa, S., and Yashima, M. (2015). Application of three-coordinate copper(I) complexes with halide ligands in organic light-emitting diodes that exhibit delayed fluorescence. *Dalton Trans.* 44: 8369–8378.

43 Igawa, S., Hashimoto, M., Kawata, I., Yashima, M., Hoshino, M., and Osawa, M. (2013). Highly efficient green organic light-emitting diodes containing luminescent tetrahedral copper(I) complexes. *J. Mater. Chem. C* 1: 542–551.

44 Hashimoto, M., Igawa, S., Yashima, M., Kawata, I., Hoshino, M., and Osawa, M. (2011). Highly efficient green organic light-emitting diodes containing luminescent three-coordinate copper(I) complexes. *J. Am. Chem. Soc.* 133: 10348–10351.

45 Wei, F., Qiu, J., Liu, X., Wang, J., Wei, H., Wang, Z., Liu, Z., Bian, Z., Lu, Z., Zhao, Y., and Huang, C. (2014). Efficient orange–red phosphorescent organic light-emitting diodes using an in situ synthesized copper(I) complex as the emitter. *J. Mater. Chem. C* 2: 6333–6341.

46 Deaton, J.C., Switalski, S.C., Kondakov, D.Y., Young, R.H., Pawlik, T.D., Giesen, D.J., Harkins, S.B., Miller, A.J.M., Mickenberg, S.F., and Peters, J.C. (2010). E-type delayed fluorescence of a phosphine-supported $Cu_2(\mu\text{-}NAr_2)_2$ diamond core: harvesting singlet and triplet excitons in OLEDs. *J. Am. Chem. Soc.* 132: 9499–9508.

47 Zhang, Q., Komino, T., Huang, S., Matsunami, S., Goushi, K., and Adachi, C. (2012). Triplet exciton confinement in green organic light-emitting diodes containing luminescent charge-transfer Cu(I) complexes. *Adv. Funct. Mater.* 22: 2327–2336.

48 Cheng, G., So, G.K.-M., To, W.-P., Chen, Y., Kwok, C.-C., Ma, C., Guan, X., Chang, X., Kwok, W.-M., and Che, C.-M. (2015). Luminescent zinc(II) and copper(I) complexes for high-performance solution-processed monochromic and white organic light-emitting devices. *Chem. Sci.* 6: 4623–4635.

49 Zhang, Q., Chen, X.-L., Chen, J., Wu, X.-Y., Yu, R., and Lu, C.-Z. (2015). Four highly efficient cuprous complexes and their applications in solution-processed organic light-emitting diodes. *RSC Adv.* 5: 34424–34431.

50 Chen, X.-L., Yu, R., Zhang, Q.-K., Zhou, L.-J., Wu, X.-Y., Zhang, Q., and Lu, C.-Z. (2013). Rational design of strongly blue-emitting cuprous

complexes with thermally activated delayed fluorescence and application in solution-processed OLEDs. *Chem. Mater.* 25: 3910–3920.

51 Yersin, H., Monkowius, U., and Czerwieniec, R. (2010). Singulett-Harvesting mit löslichen Kupfer(I)-Komplexen für opto-elektronische Vorrichtungen. Patent DE 102010031831 A1.

52 Yersin, H., Monkowius, U., and Czerwieniec, R. (2011). Copper(I) complexes for opto-electronic devices. Patent WO 2012010650 A1.

53 Medina-Rodriguez, S., Orriach-Fernandez, F.J., Poole, C., Kumar, P., de la Torre-Vega, A., Fernandez-Sanchez, J.F., Baranoff, E., and Fernandez-Gutierrez, A. (2015). Copper(I) complexes as alternatives to iridium(III) complexes for highly efficient oxygen sensing. *Chem. Commun.* 51: 11401–11404.

54 Smith, C.S., Branham, C.W., Marquardt, B.J., and Mann, K.R. (2010). Oxygen gas sensing by luminescence quenching in crystals of Cu(xantphos)(phen)$^+$ complexes. *J. Am. Chem. Soc.* 132: 14079–14085.

55 Smith, C.S. and Mann, K.R. (2012). Exceptionally long-lived luminescence from [Cu(I)(isocyanide)$_2$(phen)]$^+$ complexes in nanoporous crystals enables remarkable oxygen gas sensing. *J. Am. Chem. Soc.* 134: 8786–8789.

56 Czerwieniec, R., Leitl, M., and Yersin, H. (2013). Optical oxygen sensors with copper(I) complexes. Patent DE 102012101067 A1, Patent WO 2013117460 A2.

57 Prokhorov, A.M., Hofbeck, T., Czerwieniec, R., Suleymanova, A.F., Kozhevnikov, D.N., and Yersin, H. (2014). Brightly luminescent Pt(II) pincer complexes with a sterically demanding carboranyl-phenylpyridine ligand: A new material class for diverse optoelectronic applications. *J. Am. Chem. Soc.* 136: 9637–9642.

58 Hofbeck, T., Lam, Y.C., Kalbáč, M., Záliš, S., Vlček, A., and Yersin, H. (2016). Thermally tunable dual emission of the d^8–d^8 dimer $[Pt_2(\mu\text{-}P_2O_5(BF_2)_2)_4]^{4-}$. *Inorg. Chem.* 55: 2441–2449.

59 Mak, C.S.K., Pentlehner, D., Stich, M., Wolfbeis, O.S., Chan, W.K., and Yersin, H. (2009). Exceptional oxygen sensing capabilities and triplet state properties of Ir(ppy-NPh$_2$)$_3$. *Chem. Mater.* 21: 2173–2175.

60 Knorn, M., Rawner, T., Czerwieniec, R., and Reiser, O. (2015). [Copper(phenanthroline)(bisisonitrile)]$^+$-complexes for the visible-light-mediated atom transfer radical addition and allylation reactions. *ACS Catal.* 5: 5186–5193.

61 Tang, X.-J. and Dolbier, W.R. (2015). Efficient Cu-catalyzed atom transfer radical addition reactions of fluoroalkylsulfonyl chlorides with electron-deficient alkenes induced by visible light. *Angew. Chem. Int. Ed.* 54: 4246–4249.

62 Bagal, D.B., Kachkovskyi, G., Knorn, M., Rawner, T., Bhanage, B.M., and Reiser, O. (2015). Trifluoromethylchlorosulfonylation of alkenes: evidence for an inner-sphere mechanism by a copper phenanthroline photoredox catalyst. *Angew. Chem. Int. Ed.* 54: 6999–7002.

63 Wang, B., Shelar, D.P., Han, X.-Z., Li, T.-T., Guan, X., Lu, W., Liu, K., Chen, Y., Fu, W.-F., and Che, C.-M. (2015). Long-lived excited states of zwitterionic

copper(I) complexes for photoinduced cross-dehydrogenative coupling reactions. *Chem. Eur. J.* 21: 1184–1190.

64 Yang, Q., Dumur, F., Morlet-Savary, F., Poly, J., and Lalevée, J. (2015). Photocatalyzed Cu-based ATRP involving an oxidative quenching mechanism under visible light. *Macromolecules* 48: 1972–1980.

65 Baralle, A., Fensterbank, L., Goddard, J.-P., and Ollivier, C. (2013). Aryl radical formation by copper(I) photocatalyzed reduction of diaryliodonium salts: NMR evidence for a Cu^{II}/Cu^{I} mechanism. *Chem. Eur. J.* 19: 10809–10813.

66 Luo, S.-P., Mejía, E., Friedrich, A., Pazidis, A., Junge, H., Surkus, A.-E., Jackstell, R., Denurra, S., Gladiali, S., Lochbrunner, S., and Beller, M. (2013). Photocatalytic water reduction with copper-based photosensitizers: a noble-metal-free system. *Angew. Chem. Int. Ed.* 52: 419–423.

67 Yersin, H. (2004). Triplet emitters for OLED applications. Mechanisms of exciton trapping and control of emission properties. *Top. Curr. Chem.* 241: 1–26.

68 Helfrich, W. and Schneider, W.G. (1966). Transients of volume-controlled current and of recombination radiation in anthracene. *J. Chem. Phys.* 44: 2902–2909.

69 Yersin, H. and Finkenzeller, W.J. (2008). Triplet emitters for organic light emitting diodes: basic properties. In: *Highly Efficient OLEDs with Phosphorescent Materials* (ed. H. Yersin), 1–97. Weinheim: Wiley-VCH.

70 Yersin, H., Rausch, A.F., Czerwieniec, R., Hofbeck, T., and Fischer, T. (2011). The triplet state of organo-transition metal compounds. Triplet harvesting and singlet harvesting for efficient OLEDs. *Coord. Chem. Rev.* 255: 2622–2652.

71 Rausch, A.F., Homeier, H.H.H., and Yersin, H. (2010). Organometallic Pt(II) and Ir(III) triplet emitters for OLED applications and the role of spin–orbit coupling: a study based on high-resolution optical spectroscopy. *Top. Organomet. Chem.* 29: 193–235.

72 Rausch, A.F., Homeier, H.H.H., Djurovich, P.I., Thompson, M.E., and Yersin, H. (2007). Spin–orbit coupling routes and OLED performance – studies of blue-light emitting Ir(III) and Pt(II) complexes. *Proc. SPIE* 6655: doi: 10.1117/12.731225.

73 Azumi, T. and Miki, H. (1997). Spectroscopy of the spin sublevels of transition metal complexes. In: *Electronic and Vibronic Spectra of Transition Metal Complexes II* (ed. H. Yersin), 1–40. Berlin, Heidelberg: Springer.

74 Miki, H., Shimada, M., Azumi, T., Brozik, J.A., and Crosby, G.A. (1993). Effect of the ligand-field strength on the radiative properties of the ligand-localized $^3\pi\pi^*$ state of rhodium complexes with 1,10-phenanthroline. Proposed role of dd states. *J. Phys. Chem.* 97: 11175–11179.

75 Kimachi, S., Satomi, R., Miki, H., Maeda, K., Azumi, T., and Onishi, M. (1997). Excited-state properties of the ligand-localized $^3\pi\pi^*$ state of cyclometalated ruthenium(II) complexes. *J. Phys. Chem. A* 101: 345–349.

76 Obara, S., Itabashi, M., Okuda, F., Tamaki, S., Tanabe, Y., Ishii, Y., Nozaki, K., and Haga, M.-A. (2006). Highly phosphorescent iridium complexes containing both tridentate bis(benzimidazolyl)-benzene or -pyridine and bidentate

phenylpyridine: synthesis, photophysical properties, and theoretical study of Ir-Bis(benzimidazolyl)benzene complex. *Inorg. Chem.* 45: 8907–8921.

77 Abedin-Siddique, Z., Ohno, T., Nozaki, K., and Tsubomura, T. (2004). Intense fluorescence of metal-to-ligand charge transfer in [Pt(0)(binap)$_2$] [binap = 2,2′-bis(diphenylphosphino)-1,1′-binaphthyl]. *Inorg. Chem.* 43: 663–673.

78 Baldo, M.A., O'Brien, D.F., You, Y., Shoustikov, A., Sibley, S., Thompson, M.E., and Forrest, S.R. (1998). Highly efficient phosphorescent emission from organic electroluminescent devices. *Nature* 395: 151–154.

79 Baldo, M.A., Lamansky, S., Burrows, P.E., Thompson, M.E., and Forrest, S.R. (1999). Very high-efficiency green organic light-emitting devices based on electrophosphorescence. *Appl. Phys. Lett.* 75: 4–6.

80 Kawamura, Y., Goushi, K., Brooks, J., Brown, J.J., Sasabe, H., and Adachi, C. (2005). 100% phosphorescence quantum efficiency of Ir(III) complexes in organic semiconductor films. *Appl. Phys. Lett.* 86: 071104.

81 Sasabe, H., Takamatsu, J.-I., Motoyama, T., Watanabe, S., Wagenblast, G., Langer, N., Molt, O., Fuchs, E., Lennartz, C., and Kido, J. (2010). High-efficiency blue and white organic light-emitting devices incorporating a blue iridium carbene complex. *Adv. Mater.* 22: 5003–5007.

82 Li, K., Ming Tong, G.S., Wan, Q., Cheng, G., Tong, W.Y., Ang, W.H., Kwong, W.L., and Che, C.M. (2016). Highly phosphorescent platinum(II) emitters: photophysics, materials and biological applications. *Chem. Sci.* 7: 1653–1673.

83 Cheng, G., Kui, S.C.F., Ang, W.-H., Ko, M.-Y., Chow, P.-K., Kwong, C.-L., Kwok, C.-C., Ma, C., Guan, X., Low, K.-H., Su, S.-J., and Che, C.-M. (2014). Structurally robust phosphorescent [Pt(O^N^C^N)] emitters for high performance organic light-emitting devices with power efficiency up to 126 lm W^{-1} and external quantum efficiency over 20%. *Chem. Sci.* 5: 4819–4830.

84 Gildea, L.F. and Williams, J.A.G. (2013). Iridium and platinum complexes for OLEDs. In: *Organic Light-Emitting Diodes: Materials, Devices and Applications* (ed. A. Buckley), 77–113. Cambridge: Woodhead Publishing.

85 Zysman-Colman, E. (2017). *Iridium (III) in Optoelectronic and Photonics Applications*. Weinheim: Wiley-VCH.

86 Deaton, J.C. and Castellano, F.N. (2017). Archetypal iridium(III) compounds for optoelectronic and photonic applications. In: *Iridium (III) in Optoelectronic and Photonics Applications* (ed. E. Zysman-Colman), 1–69. Weinheim: Wiley-VCH.

87 Yersin, H. and Kratzer, C. (2002). Energy transfer and harvesting in [$Ru_{1-x}Os_x$(bpy)$_3$](PF_6)$_2$ and {Λ-[Ru(bpy)$_3$]Δ-[Os(bpy)$_3$]}(PF_6)$_4$. *Coord. Chem. Rev.* 229: 75–93.

88 Yersin, H. and Donges, D. (2001). Low-lying electronic states and photophysical properties of organometallic Pd(II) and Pt(II) compounds. Modern research trends presented in detailed case studies. In: *Transition Metal and Rare Earth Compounds: Excited States, Transitions, Interactions II* (ed. H. Yersin), 81–186. Berlin, Heidelberg: Springer.

89 Hofbeck, T. and Yersin, H. (2010). The triplet state of *fac*-Ir(ppy)$_3$. *Inorg. Chem.* 49: 9290–9299.

90 Hedley, G.J., Ruseckas, A., and Samuel, I.D.W. (2008). Ultrafast luminescence in $Ir(ppy)_3$. *Chem. Phys. Lett.* 450: 292–296.

91 Daniels, R.E., Culham, S., Hunter, M., Durrant, M.C., Probert, M.R., Clegg, W., Williams, J.A., and Kozhevnikov, V.N. (2016). When two are better than one: bright phosphorescence from non-stereogenic dinuclear iridium(III) complexes. *Dalton Trans.* 45: 6949–6962.

92 Czerwieniec, R., Kowalski, K., and Yersin, H. (2013). Highly efficient thermally activated fluorescence of a new rigid Cu(I) complex $[Cu(dmp)(phanephos)]^+$. *Dalton Trans.* 42: 9826–9830.

93 Volz, D., Wallesch, M., Flechon, C., Danz, M., Verma, A., Navarro, J.M., Zink, D.M., Bräse, S., and Baumann, T. (2015). From iridium and platinum to copper and carbon: new avenues for more sustainability in organic light-emitting diodes. *Green Chem.* 17: 1988–2011.

94 Yersin, H. and Monkowius, U. (2008). Komplexe mit kleinen Singulett-Triplett-Energie-Abständen zur Verwendung in opto-elektronischen Bauteilen (Singulett-Harvesting-Effekt). Internal patent filing, University of Regensburg 2006. German Patent DE 10 2008 033563.

95 Czerwieniec, R., Yu, J., and Yersin, H. (2011). Blue-light emission of Cu(I) complexes and singlet harvesting. *Inorg. Chem.* 50: 8293–8301.

96 Czerwieniec, R. and Yersin, H. (2015). Diversity of copper(I) complexes showing thermally activated delayed fluorescence: basic photophysical analysis. *Inorg. Chem.* 54: 4322–4327.

97 Hofbeck, T., Monkowius, U., and Yersin, H. (2015). Highly efficient luminescence of Cu(I) compounds: thermally activated delayed fluorescence combined with short-lived phosphorescence. *J. Am. Chem. Soc.* 137: 399–404.

98 Ohara, H., Kobayashi, A., and Kato, M. (2014). Simple and extremely efficient blue emitters based on mononuclear Cu(I)-halide complexes with delayed fluorescence. *Dalton Trans.* 43: 17317–17323.

99 Bergmann, L., Friedrichs, J., Mydlak, M., Baumann, T., Nieger, M., and Bräse, S. (2013). Outstanding luminescence from neutral copper(I) complexes with pyridyl-tetrazolate and phosphine ligands. *Chem. Commun.* 49: 6501–6503.

100 Tsuboyama, A., Kuge, K., Furugori, M., Okada, S., Hoshino, M., and Ueno, K. (2007). Photophysical properties of highly luminescent copper(I) halide complexes chelated with 1,2-bis(diphenylphosphino)benzene. *Inorg. Chem.* 46: 1992–2001.

101 Cuttell, D.G., Kuang, S.M., Fanwick, P.E., McMillin, D.R., and Walton, R.A. (2002). Simple Cu(I) complexes with unprecedented excited-state lifetimes. *J. Am. Chem. Soc.* 124: 6–7.

102 Kang, L., Chen, J., Teng, T., Chen, X.L., Yu, R., and Lu, C.Z. (2015). Experimental and theoretical studies of highly emissive dinuclear Cu(I) halide complexes with delayed fluorescence. *Dalton Trans.* 44: 11649–11659.

103 Zink, D.M., Bächle, M., Baumann, T., Nieger, M., Kühn, M., Wang, C., Klopper, W., Monkowius, U., Hofbeck, T., Yersin, H., and Bräse, S. (2013). Synthesis, structure, and characterization of dinuclear copper(I) halide complexes with P^N ligands featuring exciting photoluminescence properties. *Inorg. Chem.* 52: 2292–2305.

104 Chen, J., Teng, T., Kang, L., Chen, X.-L., Wu, X.-Y., Yu, R., and Lu, C.-Z. (2016). Highly efficient thermally activated delayed fluorescence in dinuclear Ag(I) complexes with a bis-bidentate tetraphosphane bridging ligand. *Inorg. Chem.* 55: 9528–9536.

105 Chen, X.L., Yu, R., Wu, X.Y., Liang, D., Jia, J.H., and Lu, C.Z. (2016). A strongly greenish-blue-emitting Cu_4Cl_4 cluster with an efficient spin–orbit coupling (SOC): fast phosphorescence: versus thermally activated delayed fluorescence. *Chem. Commun.* 52: 6288–6291.

106 Osawa, M., Kawata, I., Ishii, R., Igawa, S., Hashimoto, M., and Hoshino, M. (2013). Application of neutral d^{10} coinage metal complexes with an anionic bidentate ligand in delayed fluorescence-type organic light-emitting diodes. *J. Mater. Chem. C* 1: 4375–4383.

107 Yersin, H., Leitl, M.J., and Czerwieniec, R. (2014). TADF for singlet harvesting – next generation OLED materials based on brightly green and blue emitting Cu(I) and Ag(I) compounds. *Proc. SPIE* 9183: doi: 10.1117/12.2061010.

108 Shafikov, M.Z., Suleymanova, A.F., Czerwieniec, R., and Yersin, H. (2017). Design strategy for Ag(I)-based thermally activated delayed fluorescence reaching an efficiency breakthrough. *Chem. Mater.* 29: 1708–1715.

109 Shafikov, M.Z., Suleymanova, A.F., Czerwieniec, R., and Yersin, H. (2017). Thermally activated delayed fluorescence from Ag(I) complexes: a route to 100% quantum yield at unprecedently short decay time. *Inorg. Chem.* 56: 13274–13285.

110 Uoyama, H., Goushi, K., Shizu, K., Nomura, H., and Adachi, C. (2012). Highly efficient organic light-emitting diodes from delayed fluorescence. *Nature* 492: 234–238.

111 Zhang, Q., Li, B., Huang, S., Nomura, H., Tanaka, H., and Adachi, C. (2014). Efficient blue organic light-emitting diodes employing thermally activated delayed fluorescence. *Nat. Photonics* 8: 326–332.

112 Kaji, H., Suzuki, H., Fukushima, T., Shizu, K., Suzuki, K., Kubo, S., Komino, T., Oiwa, H., Suzuki, F., Wakamiya, A., Murata, Y., and Adachi, C. (2015). Purely organic electroluminescent material realizing 100% conversion from electricity to light. *Nat. Commun.* 6: 8476.

113 Cui, L.-S., Nomura, H., Geng, Y., Kim, J.U., Nakanotani, H., and Adachi, C. (2017). Controlling singlet–triplet energy splitting for deep-blue thermally activated delayed fluorescence emitters. *Angew. Chem. Int. Ed.* 56: 1571–1575.

114 McMillin, D.R. and McNett, K.M. (1998). Photoprocesses of copper complexes that bind to DNA. *Chem. Rev.* 98: 1201–1220.

115 Mara, M.W., Fransted, K.A., and Chen, L.X. (2015). Interplays of excited state structures and dynamics in copper(I) diimine complexes: implications and perspectives. *Coord. Chem. Rev.* 282–283: 2–18.

116 Chen, L.X., Jennings, G., Liu, T., Gosztola, D.J., Hessler, J.P., Scaltrito, D.V., and Meyer, G.J. (2002). Rapid excited-state structural reorganization captured by pulsed X-rays. *J. Am. Chem. Soc.* 124: 10861–10867.

117 Chen, L.X., Shaw, G.B., Novozhilova, I., Liu, T., Jennings, G., Attenkofer, K., Meyer, G.J., and Coppens, P. (2003). MLCT state structure and dynamics of

a copper(I) diimine complex characterized by pump–probe X-ray and laser spectroscopies and DFT calculations. *J. Am. Chem. Soc.* 125: 7022–7034.

118 Iwamura, M., Watanabe, H., Ishii, K., Takeuchi, S., and Tahara, T. (2011). Coherent nuclear dynamics in ultrafast photoinduced structural change of bis(diimine)copper(I) complex. *J. Am. Chem. Soc.* 133: 7728–7736.

119 Lavie-Cambot, A., Cantuel, M., Leydet, Y., Jonusauskas, G., Bassani, D.M., and McClenaghan, N.D. (2008). Improving the photophysical properties of copper(I) bis(phenanthroline) complexes. *Coord. Chem. Rev.* 252: 2572–2584.

120 Armaroli, N., Accorsi, G., Cardinali, F., and Listorti, A. (2007). Photochemistry and photophysics of coordination compounds: copper. In: *Photochemistry and Photophysics of Coordination Compounds I* (ed. V. Balzani and S. Campagna), 69–115. Berlin, Heidelberg: Springer.

121 Iwamura, M., Takeuchi, S., and Tahara, T. (2015). Ultrafast excited-state dynamics of copper(I) complexes. *Acc. Chem. Res.* 48: 782–791.

122 Garakyaraghi, S., Danilov, E.O., McCusker, C.E., and Castellano, F.N. (2015). Transient absorption dynamics of sterically congested Cu(I) MLCT excited states. *J. Phys. Chem. A* 119: 3181–3193.

123 Siddique, Z.A., Yamamoto, Y., Ohno, T., and Nozaki, K. (2003). Structure-dependent photophysical properties of singlet and triplet metal-to-ligand charge transfer states in copper(I) bis(diimine) compounds. *Inorg. Chem.* 42: 6366–6378.

124 Turro, N.J., Ramamurthy, V., and Scaiano, J.C. (2010). *Modern Molecular Photochemistry of Organic Molecules*. University Science Books.

125 Siebrand, W. (1967). Radiationless transitions in polyatomic molecules. I. Calculation of Franck–Condon factors. *J. Chem. Phys.* 46: 440–447.

126 Robinson, G.W. and Frosch, R.P. (1963). Electronic excitation transfer and relaxation. *J. Chem. Phys.* 38: 1187–1203.

127 McCusker, C.E. and Castellano, F.N. (2013). Design of a long-lifetime, earth-abundant, aqueous compatible Cu(I) photosensitizer using cooperative steric effects. *Inorg. Chem.* 52: 8114–8120.

128 Atkins, P.W. (1991). *Quanta: A Handbook of Concepts*. Oxford University Press.

129 Barltrop, J.A. and Coyle, J.D. (1975). *Excited States in Organic Chemistry*. Wiley.

130 Szabo, A. and Ostlund, N.S. (1989). *Modern Quantum Chemistry: Introduction to Advanced Electronic Structure Theory*. Dover Publications.

131 Parker, C.A. and Hatchard, C.G. (1961). Triplet-singlet emission in fluid solutions. Phosphorescence of eosin. *Trans. Faraday Soc.* 57: 1894–1904.

132 Parker, C.A. and Hatchard, C.G. (1962). Triplet-singlet emission in fluid solution. *J. Phys. Chem.* 66: 2506–2511.

133 Bergmann, L., Hedley, G.J., Baumann, T., Bräse, S., and Samuel, I.D. (2016). Direct observation of intersystem crossing in a thermally activated delayed fluorescence copper complex in the solid state. *Sci. Adv.* 2: e1500889.

134 Ma, C., Kwok, W.-M., Czerwieniec, R., and Yersin, H. Manuscript in Preparation.

135 Gneuss, T., Leitl, M.J., Finger, L.H., Yersin, H., and Sundermeyer, J. (2015). A new class of deep-blue emitting Cu(I) compounds – effects of counter ions on the emission behavior. *Dalton Trans.* 44: 20045–20055.

136 Gneuss, T., Leitl, M.J., Finger, L.H., Rau, N., Yersin, H., and Sundermeyer, J. (2015). A new class of luminescent Cu(I) complexes with tripodal ligands – TADF emitters for the yellow to red color range. *Dalton Trans.* 44: 8506–8520.

137 Yersin, H. and Strasser, J. (2000). Triplets in metal–organic compounds. Chemical tunability of relaxation dynamics. *Coord. Chem. Rev.* 208: 331–364.

138 Yersin, H., Humbs, W., and Strasser, J. (1997). Characterization of excited electronic and vibronic states of platinum metal compounds with chelate ligands by highly frequency-resolved and time-resolved spectra. *Top. Curr. Chem.* 191: 153–249.

139 Tinti, D.S. and El-Sayed, M.A. (1971). New techniques in triplet state phosphorescence spectroscopy: application to the emission of 2,3-dichloroquinoxaline. *J. Chem. Phys.* 54: 2529–2549.

140 Harrigan, R.W. and Crosby, G.A. (1973). Symmetry assignments of the lowest CT excited states of ruthenium(II) complexes via a proposed electronic coupling model. *J. Chem. Phys.* 59: 3468–3476.

141 Hager, G.D. and Crosby, G.A. (1975). Charge-transfer exited states of ruthenium(II) complexes. I. Quantum yield and decay measurements. *J. Am. Chem. Soc.* 97: 7031–7037.

142 Azumi, T., O'Donnell, C.M., and McGlynn, S.P. (1966). On the multiplicity of the phosphorescent state of organic molecules. *J. Chem. Phys.* 45: 2735–2742.

143 Finkenzeller, W.J. and Yersin, H. (2003). Emission of $Ir(ppy)_3$. Temperature dependence, decay dynamics, and magnetic field properties. *Chem. Phys. Lett.* 377: 299–305.

144 Yersin, H., Leitl, M.J., Hofbeck, T., Czerwieniec, R., and Monkowius, U. (2013). Extended singlet harvesting for OLEDs and other electronic devices. Patent DE 102013106426 A1, Patent WO 2014202675 A1.

145 Yersin, H., Humbs, W., and Strasser, J. (1997). Low-lying electronic states of $[Rh(bpy)_3]^{3+}$, $[Pt(bpy)_2]^{2+}$, and $[Ru(bpy)_3]^{2+}$. A comparative study based on highly resolved and time-resolved spectra. *Coord. Chem. Rev.* 159: 325–358.

146 Czerwieniec, R., El-Naggar, A.M., Albassam, A.A., Kityk, I.V., Graf, M., and Yersin, H. (2015). Electric-field induced nonlinear optical materials based on a bipolar copper (I) complex embedded in polymer matrices. *J. Mater. Sci. Mater. Electron.* 26: 8394–8397.

147 Yersin, H., Czerwieniec, R., and Hupfer, A. (2012). Singlet harvesting with brightly emitting Cu(I) and metal-free organic compounds. *Proc. SPIE* 8435: doi: 10.1117/12.921372.

148 Yersin, H., Monkowius, U., Czerwieniec, R., and Yu, J. (2009). Patent DE 102008048336 A1 (2008) Patent WO 2010031485 A1 (2009).

149 Krylova, V.A., Djurovich, P.I., Conley, B.L., Haiges, R., Whited, M.T., Williams, T.J., and Thompson, M.E. (2014). Control of emission colour with N-heterocyclic carbene (NHC) ligands in phosphorescent three-coordinate Cu(I) complexes. *Chem. Commun.* 50: 7176–7179.

150 Yersin, H., Monkowius, U., and Hofbeck, T. (2013). Patent DE 102011080240 (2011), Patent WO 2013017675 (2013).

151 Czerwieniec, R. and Yersin, H. (2014). Patent DE 102013100181 (2013), Patent WO 2014108430 (2014).

152 Becke, A.D. (1993). A new mixing of Hartree–Fock and local density-functional theories. *J. Chem. Phys.* 98: 1372–1377.

153 Weigend, F. and Ahlrichs, R. (2005). Balanced basis sets of split valence, triple zeta valence and quadruple zeta valence quality for H to Rn: design and assessment of accuracy. *Phys. Chem. Chem. Phys.* 7: 3297–3305.

154 Shaw, G.B., Grant, C.D., Shirota, H., Castner, E.W., Meyer, G.J., and Chen, L.X. (2007). Ultrafast structural rearrangements in the MLCT excited state for copper(I) bis-phenanthrolines in solution. *J. Am. Chem. Soc.* 129: 2147–2160.

155 Vorontsov, I.I., Graber, T., Kovalevsky, A.Y., Novozhilova, I.V., Gembicky, M., Chen, Y.-S., and Coppens, P. (2009). Capturing and analyzing the excited-state structure of a Cu(I) phenanthroline complex by time-resolved diffraction and theoretical calculations. *J. Am. Chem. Soc.* 131: 6566–6573.

156 Hua, L., Iwamura, M., Takeuchi, S., and Tahara, T. (2015). The substituent effect on the MLCT excited state dynamics of Cu(I) complexes studied by femtosecond time-resolved absorption and observation of coherent nuclear wavepacket motion. *Phys. Chem. Chem. Phys.* 17: 2067–2077.

157 Papanikolaou, P.A. and Tkachenko, N.V. (2013). Probing the excited state dynamics of a new family of Cu(I)-complexes with an enhanced light absorption capacity: excitation-wavelength dependent population of states through branching. *Phys. Chem. Chem. Phys.* 15: 13128–13136.

158 Tschierlei, S., Karnahl, M., Rockstroh, N., Junge, H., Beller, M., and Lochbrunner, S. (2014). Substitution-controlled excited state processes in heteroleptic copper(I) photosensitizers used in hydrogen evolving systems. *ChemPhysChem* 15: 3709–3713.

159 Strickler, S.J. and Berg, R.A. (1962). Relationship between absorption intensity and fluorescence lifetime of molecules. *J. Chem. Phys.* 37: 814–822.

160 Schmidt, J., Wiedenhofer, H., von Zelewsky, A., and Yersin, H. (1995). Time-resolved vibrational structures of the triplet sublevel emission of $Pd(2\text{-thpy})_2$. *J. Phys. Chem.* 99: 226–229.

161 Czerwieniec, R., Finkenzeller, W.J., Hofbeck, T., Starukhin, A., Wedel, A., and Yersin, H. (2009). Photophysical properties of $Re(pbt)(CO)_4$ studied by high resolution spectroscopy. *Chem. Phys. Lett.* 468: 205–210.

162 Niehaus, T. A. and Yersin, H. Unpublished results.

163 Wallesch, M., Volz, D., Fléchon, C., Zink, D.M., Bräse, S., and Baumann, T. (2014). Bright coppertunities: efficient OLED devices with copper(I) iodide-NHetPHOS-emitters. *Proc. SPIE* 9183: doi: 10.1117/12.2060499.

164 Bizzarri, C., Strabler, C., Prock, J., Trettenbrein, B., Ruggenthaler, M., Yang, C.-H., Polo, F., Iordache, A., Brüggeller, P., and Cola, L.D. (2014). Luminescent dinuclear Cu(I) complexes containing rigid tetraphosphine ligands. *Inorg. Chem.* 53: 10944–10951.

165 Murov, S. L., Carmichael, I., and Hug, G.L. (1993). Handbook of Photochemistry, 2. Taylor & Francis, p 340.

166 McGlynn, S.P., Azumi, T., and Kinoshita, M. (1969). *Molecular Spectroscopy of the Triplet State*. Prentice-Hall.

167 El-Sayed, M.A. (1963). Spin–orbit coupling and the radiationless processes in nitrogen heterocyclics. *J. Chem. Phys.* 38: 2834–2838.

168 Leitl, M.J. (2015). *Photophysical Characterization of OLED relevant Cu(I) Complexes Exhibiting Thermally Activated Delayed Fluorescence (TADF).* Universität Regensburg.

169 McHale, J. L. *Molecular Spectroscopy*. Prentice Hall: 1999.

170 Penfold, T.J. (2015). On predicting the excited-state properties of thermally activated delayed fluorescence emitters. *J. Phys. Chem. C* 119: 13535–13544.

171 Shafikov, M.Z., Suleymanova, A.F., Schinabeck, A., and Yersin, H. (2018). Dinuclear Ag(I) complex designed for highly efficient thermally activated delayed fluorescence. *J. Phys. Chem. Lett.* 9: 702–709.

172 Kaeser, A., Moudam, O., Accorsi, G., Séguy, I., Navarro, J., Belbakra, A., Duhayon, C., Armaroli, N., Delavaux-Nicot, B., and Nierengarten, J.F. (2014). Homoleptic copper(I), silver(I), and gold(I) bisphosphine complexes. *Eur. J. Inorg. Chem.* 1345–1355.

173 Hsu, C.-W., Lin, C.-C., Chung, M.-W., Chi, Y., Lee, G.-H., Chou, P.-T., Chang, C.-H., and Chen, P.-Y. (2011). Systematic investigation of the metal-structure–photophysics relationship of emissive d^{10}-complexes of group 11 elements: the prospect of application in organic light emitting devices. *J. Am. Chem. Soc.* 133: 12085–12099.

174 Igawa, S., Hashimoto, M., Kawata, I., Hoshino, M., and Osawa, M. (2012). Photoluminescence properties, molecular structures, and theoretical study of heteroleptic silver(I) complexes containing diphosphine ligands. *Inorg. Chem.* 51: 5805–5813.

175 Hsu, C.-C., Lin, C.-C., Chou, P.-T., Lai, C.-H., Hsu, C.-W., Lin, C.-H., and Chi, Y. (2012). Harvesting highly electronically excited energy to triplet manifolds: state-dependent intersystem crossing rate in Os(II) and Ag(I) complexes. *J. Am. Chem. Soc.* 134: 7715–7724.

176 Kunkely, H. and Vogler, A. (2006). Optical properties of Ag(tripod)X with tripod = 1,1,1-tris(diphenyl-phosphinomethyl)ethane and $X^- = Cl^-$ and I^-: Intraligand and ligand-to-ligand charge transfer. *Inorg. Chim. Acta* 359: 388–390.

177 Crespo, O., Gimeno, M.C., Jones, P.G., and Laguna, A. (1996). Silver complexes with the nido-diphosphine [7,8-$(PPh_2)_2$-7,8-$C_2B_9H_{10}$]. *Dalton Trans.* 4583–4588.

178 Capano, G., Rothlisberger, U., Tavernelli, I., and Penfold, T.J. (2015). Theoretical rationalization of the emission properties of prototypical Cu(I)–phenanthroline complexes. *J. Phys. Chem. A* 119: 7026–7037.

179 Matsumoto, K., Shindo, T., Mukasa, N., Tsukuda, T., and Tsubomura, T. (2010). Luminescent mononuclear Ag(I)–bis(diphosphine) complexes: correlation between the photophysics and the structures of mononuclear Ag(I)–bis(diphosphine) complexes. *Inorg. Chem.* 49: 805–814.

180 Yersin, H., Mataranga-Popa, L., and Czerwieniec, R. (2017). *Design of organic TADF molecules. The role of $\Delta E(S_1–T_1)$: from fluorescence to TADF and beyond – towards the fourth generation OLED mechanism*. Krutyn: 22nd International Krutyn Summer School http://www.excilight.com/node/203.

181 Yersin, H., Mataranga-Popa, L., and Czerwieniec, R. (2017). Organische Moleküle für Direktes Singulett-Harvesting mit kurzer Emissionsabklingzeit zur Verwendung in opto-elektronischen Vorrichtungen. Patent EP 17170682.3.

182 Yersin, H., Mataranga-Popa, L., and Czerwieniec, R. (2017). Patent DE 102017101432.2.

183 Yersin, H., Mataranga-Popa, L., Li, S.-W., and Czerwieniec, R. (2018). Design strategies for materials showing thermally activated delayed fluorescence and beyond: Towards the fourth-generation OLED mechanism. *J. Soc. Info. Display.* 26: 194–199. doi: 10.1002/jsid.654.